Dolomite cements in Cenomanian continental sand deposits: Time evolution and significance (Zoovch Ovoo U-deposit, East Gobi Basin, Mongolia)

Dimitrios Rallakis, Raymond Michels, Marc Brouand, Olivier Parize, Michel Cathelineau

Dolomite cements in Cenomanian continental sand deposits: Time evolution and significance (Zoovch Ovoo U-deposit, East Gobi Basin, Mongolia)

Dimitrios Rallakis[1*], Raymond Michels[1], Marc Brouand[2], Olivier Parize[2] & Michel Cathelineau[1]

[*]Corresponding author, dimitrios.rallakis@univ-lorraine.fr

[1]Université de Lorraine, CNRS, CREGU, GeoRessources, F-54500 Nancy, France

[2]ORANO Mining, Le Prisme, 125 Avenue de Paris, 92320, Chatillon, France

Abstract

Shallow buried unconsolidated sands generally provide very little information about diagenesis as most detrital minerals remain unchanged. However, in rare cases carbonate cemented nodules or sandstone layers may occur inside unconsolidated series. These cements could help to reconstruct the chronology of events from early to late phase stages of diagenesis. The Late Cretaceous sequence of the Zoovch Ovoo depocenter in East Gobi Basin is represented by 600m of clastic deposits. The 60-80m of Cenomanian unconsolidated sands and clays, deposited in alluvial-deltaic to lacustrine settings, compose the upper part of the post-rift medium-grained siliciclastic reservoir, the Sainshand Formation which hosts uranium roll-front systems. Dolomite cemented sandstone layers with 10-20cm thickness occur among the unconsolidated rock facies. Calcite is absent from this formation, but is present only in the overlying, also outcropping, Bayanshiree Formation. Samples from the dolomite cemented sandstone layers were investigated in detail to uncover their origin and diagenetic history. Four dolomite cement types were recognized that indicate recrystallization episodes and were classified based on the size and shape of the crystals, namely: (i) microcrystalline dolomite frequently associated with siderite, (ii) euhedral dolomite also associated with siderite, (iii)

subhedral dolomite and (iv) finally anhedral dolomite. Their REE content varies significantly from dolomite I to IV, in particular by a strong depletion in LREE about 30 times. The contrasted precipitation of calcite in Bayanshiree and dolomite cements in Sainshand formations could be attributed to different Mg/Ca ratio of the circulation fluids in the two aquifers. Both carbonates display however rather homogenous oxygen and carbon isotopic compositions for $\delta^{18}O$ (–10±1‰ V-PDB) and $\delta^{13}C$ (–7±1‰ V-PDB). The $\delta^{18}O$ values are interpreted as inherited from typical meteoric waters quite close to present day waters. The $\delta^{13}C$ values indicate a mixed source of both organic and mineral carbon. All data taken into account, a full paragenetic succession was constructed. It includes the evolution of dolomite during burial diagenesis and the effects of the oxidizing roll-front uranium rich waters in the system. The latter induces partial dissolution followed by precipitation of a dolomite phase typical of roll-front zones. Carbonate cements can be thus considered as the best and rather unique geochemical indicators for the recognition of a burial history framework to paleofluid circulations and fluid-rock interactions in these intracontinental series of unconsolidated sands.

Keywords: Dolomite, Roll-front, Uranium, Late cretaceous, East Gobi Basin, Mongolia

1 Introduction

Models of primary dolomite cement formation (Last, 1990; Last et al., 2010; Last et al., 2012; Casado et al., 2014) in continental settings without any marine influence (Colson and Cojan, 1996; Alonso-Zarza and Martín-Pérez., 2008) have been proposed in various settings: (i) climate controlled ephemeral continental (playa) lakes with evaporation occurring during semi-arid episodes, precipitating dolomite (Cojan, 2010), (ii) progressive Ca depletion of meteoric water during surface run-off due to evaporation and groundwater infiltration, causing Mg saturation, resulting into dolocrete formation (Worden and Burley, 2003) and (iii) precipitation of pedogenic dolomite in soils in the presence of certain types of soil microbes (Roberts et al., 2004; Wright and Wacey, 2005; Sánchez-Román et al., 2004; Kearsey et al., 2012).

Most commonly siderite, ankerite and dolomite are formed along contrasted redox conditions in estuarine conditions (Humphrey, 2000). In such context, the main process is the formation of dolomite by lateral evolution of surface waters submitted to evaporation (Worden and Burley, 2003; Cojan, 2010; Kearsey et al., 2012). Factors controlling dolomite precipitation in saline wetlands submitted to arid climate are described in detail in Mather et al. (2018).

In more deeply buried series, dolomite cements are frequently related to the mixing of brackish waters and deep hydrothermal fluids, a process responsible for the dolomitization of limestones through dissolution and recrystallization cycles (Warren, 2000). This is the case also of most Mississippi Valley type deposits where extended dolomitization occurs near the boundary with basement rocks, generally in relation with the incoming of primary brines issued from sea water evaporation, typically enriched in Mg (Leach et al., 2005; Muchez et al., 2005; Boiron et al., 2010). Spirakis (1996) made a link between dolomite cemented sandstone layers associated to uranium roll-front type deposits that form at depth between the fresh water/deep water (brine) interface. In that case dolomite formation was attributed to organic matter bacterial fermentation (methanogenesis) during early diagenesis and there were also evidences for dolomite forming during the ore stage. However, the origin of local dolomite cementation in an unconsolidated continental sand sequence despite mineralized, like the one studied here, is a much less documented topic (Morad, 1990; Spötl and Wright, 1992).

In the intracontinental basins of Mongolia, recent series of drillings for uranium exploration in the fluvio-lacustrine deposits of the Cenomanian Sainshand Formation at Zoovch Ovoo revealed the presence of sporadic cemented sandstone layers within an otherwise unconsolidated sedimentary succession. The carbonate cement in the whole Sainshand Formation in the studied depocenter is exclusively dolomite and is characterized by several petrographic textures and habits. In the upper unit that is also the main outcrop in East Gobi Basin, namely the Bayanshiree Formation, dolomite is absent, whereas calcite was found mostly as joint cements. The exclusive presence of the dolomite cement at depth was thus investigated in this study as the chronology of cements and processes affecting these sands

is crucial for the understanding of the formation of the uranium deposit and also for the management of ore exploitation. The purpose of the present study was thus i) to produce a first assessment of the mineralogy and geochemistry of dolocrete within the Sainshand formation, ii) to understand the process at the origin of the different Sainshand dolomite cements, and therefore to get indications on the paleohydrological conditions, iii) to investigate why interstitial fluids were saturated with respect to dolomite throughout the whole sequence of events from sedimentation to burial and uplift and iv) to identify potential implications on uranium deposition.

2 Geological setting

The area of study is located in south-eastern Mongolia in East Gobi Basin and in particular in the Zuunbayan sub-basin and the Zoovch Ovoo district, hosting the homonymous roll-front type uranium deposit. The East Gobi Basin extends for 700 km in E-W trend and 300 km in the N-S (Meyerhoff and Meyer, 1987; Prost, 2004). It is a northeast-southwest trending continental basin of multiphase deformation (plate interior poly-phase basin) formatted by Mesozoic extension events (Johnson and Ritts, 2012).

The East Gobi Basin includes the following four morpho-tectonic elements: the Unegt sub-basin, the Zuunbayan sub-basin, the Khovsgol sub-basin and the Sainshand sub-basin (Johnson, 2004). The studied material originates from the Zuunbayan sub-basin, which is NE oriented and covers an area of 2000 km^2. Although the geometry the East Gobi Basin is not very well defined, seismic surveys reveal the presence of two depocenters, one in the vicinity and another about 50 km southwest of the Tsagaan Els oil field, respectively. The Mesozoic-Cenozoic sedimentary sequence is estimated to approach about 4000 m in thickness. The granitic outcrops in the NE and S parts of the basin, suggest the presence of quartz arenite sandstone sources (Prost, 2004; **Figure 1**).

2.1 Tectonic history

According to recent studies the East Gobi Basin was subjected to four discrete cycles of deformation and subsidence. Based on petroleum-exploration seismic profiles (Prost, 2004; Johnson and Ritts, 2012; Heumann et al., 2014) these phases lasted from Late Paleozoic to Cenozoic (**Figure 2**) and can be summarized as follows:

- The Late Permian post-collisional basin due to the closure of the Paleo-Asian Ocean. As a result the basement consists of turbiditic sequences of Permian age that are unconformably overlain by non-marine Permo-Triassic sediments (**Phase 1**).
- The Early Mesozoic transpressional foreland created by a major sinistral shear zone lasting until Late Triassic and “thrusting” Precambrian and early Paleozoic carbonate klippe (**Phase 2**).
- The Late Mesozoic rift basin lasting from Late Jurassic to Late Cretaceous, which is marked by the development of high angle normal faults (**Phase 3**).
- The Late Cretaceous post-rift succession and the development of a strike slip basin, marked by the regional unconformity and basin inversion. Although the sediments overlying the Late Cretaceous are characterized as a post-rift thermal sag phase, there were probably left lateral strike-slip faults developing during Early Cenozoic (**Phase 4**).

Finally, the Mesozoic sequence is covered by Tertiary-Quaternary fine to coarse grained low thickness alluvial sedimentation, forming anticlines of up to 5 km long and 1-2 km wide. Uplift episodes during the Early Cenozoic are also likely to have occurred as older units outcrop locally the Tertiary-Quaternary deposits (Prost, 2004), probable due to the movement of the Altyn Tagh fault in China during Oligocene-Miocene that reactivated the East Gobi Fault Zone resulting into continental extrusion (Johnson and Ritts 2012).

2.2 Lithostratigraphy

The lithostratigraphy of the East Gobi basin is presented in **Figure 3**. The base of the stratigraphy (Devonian-Permian) consists of widely spread metamorphosed Paleozoic arc-related volcanics and marine siliciclastics, setting up the Tavan Tolgoy Formation (Traynor and Sladen, 1995; Lamb and Badarch, 1997; Graham et al., 2001). The Paleozoic basement is overlain unconformably by a 1000-4000m thick sedimentary succession. The cumulative sedimentary record ranges from Jurassic to Tertiary and is composed of continental sediments (Meyerhoff and Meyer, 1987; Prost, 2004). Generally, the whole Triassic-Early Jurassic sequence is missing from the record due to repeated episodes of block faulting and multiphase deformation (Johnson, 2004; Itterbeeck et al., 2005); hence a hiatus of variable thickness exists between Permian and Middle Jurassic. The Khamar Khovoor Formation was deposited during Middle-Upper Jurassic times and is 750m thick. The depositional setting at that time was paralic to marginal marine, setting up a combination of fluvial, lacustrine, deltaic and swamp-organic sedimentation. The fluvial character is expressed by braided rivers depositing sandstones with channel shape geometry and the paralic by dominant shale deposits. The Khamar Khovoor Formation forms a hiatus with the overlying Upper Jurassic (Tithonian-Kimeridgian) Sharlyn Formation that consists of 200m of well-defined braided fluvial sandstones, conglomerates and to a lesser extent finer deposits, like lacustrine shales (Graham et al., 2001; Prost, 2004), before gradually passing to a 300-700m thick sequence consisting mainly of shales interbedded with coarser fractions (dark-colored sandstones, conglomerates, siltstones) and volcanics (red-colored tuffs, basalts) forming gradually the Tsagaan Tsav Formation of Early Cretaceous (Valanginian) age.

The Tsagaan Tsav Formation is composed of a 530 m thick fining upwards sequence of alluvial fan and braided stream deposits, which is topped by fine material deposited during flooding events (overbank deposits) and lacustrine facies (Graham et al., 2001; Johnson, 2004). The coarser sandstone part of the Tsagaan Tsav Formation is the reservoir unit for the regional Tsagaan Els and Zuunbayan oil fields. The Zuunbayan Formation is composed of

non-marine poorly compacted sandstones, interbedded with shales and volcanic tuff and is divided in three different units. The basal unit is organic rich and contains bituminous shales with petroleum source potential. The mid and upper units contain coals and sandstones with channel geometry along with basaltic flows (Prost, 2004). There is a clear unconformity between Late and Early Cretaceous that separates the Zuunbayan Formation from the Late Cretaceous (Cenomanian) Sainshand Formation, which is composed of red sandstones, claystones and conglomerates, reflecting high energy fluvial deposits. The age of the Zuunbayan Formation is Hauterivian to Albian and its thickness is around 970 m.

The Sainshand Formation, which also hosts the studied uranium deposit (Zoovch Ovoo) in the Zuunbayan sub-basin (Parize, 2013; Le Goux et al., 2015) has Cenomanian age and is 100-350m thick. It can be separated into respective sub-units that reflect different cycles of lacustrine and alluvial sedimentation setting up a combination of conglomerate, sand, silt and clay sedimentation (Dahlkamp, 2009). The Sainshand Formation is overlayed by the Late Cretaceous (Santonian-Turonian) Bayanshiree Formation, consisting mainly of reddish to grayish shales with minor input of sandstones with channel-shape geometry (Graham et al., 2001; Johnson, 2004).

Above occur two Late Cretaceous lacustrine coarse clastic units, namely the Santonian-Campanian Baruungoyot Formation and the Campanian-Maastrichtian Nemegt Formation. The Upper Cretaceous post-rift sequence was certainly deposited during a sag-basin story (sediment starvation). It has also recorded the tectonic events (strike slip tectonic) that took place during Cenozoic. The deposits related to this sequence could be strongly dipped along the faulted boundaries of these sub-basins whereas they are cropped generally flat and sub-horizontal in the syncline heart. Locally, it is possible to include Tertiary and Quaternary strata due to the re-activation of the East Gobi Fault Zone (Johnson and Ritts, 2012; Heumann et al., 2014). Although these units are generally undifferentiated with granular sizes ranging from very fine to coarse, they can locally top-up unconformably the Late Cretaceous strata (Prost, 2004).

2.3 Sampling

In the Zoovch Ovoo area the Sainshand Formation sands are locally cemented by dolomite. These dolomite cemented sandstones (56 recognized layers) were sampled from drill-cores at depths between 120 and 200m targeting the uraniferous sequence of Sainshand Formation both randomly from appraisal wells and systematically along profiles i.e. A-B (**Figure 4**). The thickness of the dolomite cemented sandstone layers from which each studied sample was recovered is low (10-20cm), while the remaining of the core succession is represented by poorly to non-consolidated sediments. The grain size of the dolomite cemented sandstones ranges from medium fine grained to very coarse grained and sometimes contain dolomite granules. According to their position to the roll-front the sediments can be oxidized, oxidized/reduced or reduced, indicating post roll-front, on-going roll-front and pre roll-front activity. Dolomite cements occur both within the reduced and the oxidized part of the roll-front.

The lateral extension of the cemented facies is unknown, but does not reach the distance in between two wells and as a result the carbonate layers could not be correlated. Profile B is richer in dolomite occurrences than Profile A. With respect to their position in the roll-front, Profile B is located in the middle, at the crest of the roll-front, while Profile A is displaced about 2.5 km towards the east (**Figure 4**). In general, dolomite cemented sandstones are “bounding” the mineralization zone except for three samples that are located inside the zone, namely: A-36, B-37 and B-133.

Calcite was never encountered at depth in Zoovch Ovoo (Sainshand Formation), but a few calcite samples were recovered from outcrops of the Bayanshiree Formation (Turonian), at the vicinity of the East Hongor Tolgoy and Bayanshiree Plateau (**Figure 1**). The calcite samples occur as cement in sandstones or concretions, the latter case referring to pure calcite (absence of sand grains).

2.4 Petrography and crystal-chemistry

Polished thin sections (~30 µm thick) were prepared and were studied using optical microscopy (in transmitted and reflected light modes). Classification of the samples follows indications by Dott (1964) for mineral associations and Wentworth (1922) for granulometry.

Cathodoluminescence images of carbonates were obtained using a CATHODYNE OPEA optical microscope in GeoRessources Nancy. Mineral semi-quantitative analysis and determinations were carried out using a PHILIPS XL30 Scanning Electron Microscope (SEM), equipped with an energy dispersive spectrometer using a Si-(Li) semi-conductor detector, coupled with a HITACHI S-4800 scanning electron microscope (SEM) in GeoRessources, Nancy.

The electron probe micro-analyzer (EPMA) is one of the most widely analytical tools to be used in order to evaluate dolomite composition (Rosen et al., 1988; Omer at al., 2014). A CAMECA SX100 (GeoRessources, Nancy) was used, the calibration been made using natural and synthetic oxides or alloys (orthoclase, albite, $MnTiO_3$, wollastonite, hematite and olivine). The analytical conditions were: 10 nA current, 15 kV accelerating voltage, 10 s counting time for (K, Na, Ca), 20 s for (Al, Fe, Mn) and 40 s for (Mg, U).

For the bulk rock geochemistry, the samples were initially dissolved in a microwave oven Milestone MLS 1200 Mega, using a solution of HF-$HClO_4$-HNO_3-H_2O_2 (Cheburkin and Shotyk, 1996). The concentrations of the major elements (Ca, Fe, K, Mg and Na) were determined by Atomic Absorption Spectroscopy (AAS), and the trace elements (As, B, Ba, Co, Cr, Cu, Ga, Mn, Mo, Ni, Pb, Rb, Sr, U, V, Zn and REE) by Inductively Coupled Mass Spectroscopy (ICP-MS). The analyses were performed in CRPG, Nancy.

The XRD analysis of bulk rock powder of carbonate cemented sandstones and on oriented clay extracts were obtained using a Bruker D2 Phaser equipped with a LynxEye XE-T detector, in GeoRessources, Nancy. The interpretation software package used for the evaluation of the diffractograms was Diffrac.Suite along with EVA.

2.5 Rare earth elements of carbonates

Laser Ablation-Inductively Coupled Plasma Mass Spectrometry (LA-ICPMS) available at GeoRessources was used to determine the Rare Earth Elements contents (REEs) in dolomite cements and calcite samples in GeoRessources, Nancy. Objective was to compare the spectra between the carbonate cement generations with respect to the relative REE abundance as well as to the relative enrichment or depletion of certain elements i.e. europium, which gives information on redox conditions at the time of formation (Fowler and Doig, 1982). These features may help in observing geochemical trends which would allow further distinctions between the carbonate generations. Laser sampling was performed with a 193 nm GeoLas Pro ArF Excimer laser (Microlas®, Göttingen, Germany) equipped with beam homogenization optics. Ablation was performed by focusing the beam at the sample surface with a constant fluency of 10 J/cm^2 and constant repetition rate of 5 Hz. Helium was used as a carrier gas to transport the laser generated aerosols from the ablation cell to the ICP-MS. Ablated material was analyzed by an Agilent 7500c Quadrupole ICP-MS (Agilent®, Santa Clara, California) equipped with an Octopole Reaction System with enhanced sensitivity optional lenses (Cs type, Agilent).

The certified glass standards NIST610, NIST612 and NIST614 SRM were used as reference materials (concentrations from Pearce et al., 1997) for the calibration of the LA-ICP-MS. The protocol for routine analysis of REE in carbonate was checked using GSR6 reference carbonate standard (Xie et al., 1989). Absolute concentrations and limit of detection were obtained from the equations developed by Longerich et al. (1996). The suite of elements analyzed by LA-ICP-MS is, La, Ce, Pr, Nd, Sm, Eu, Gd, Tb, Dy, Ho, Er, Tm, Yb, and Lu. The detection limit range from a few ppm for Ce to down to 0.5 ppm for heavy rare earth elements. The REE spectra were normalized to PAAS (McLennan, 1989).

2.6 Stable isotopes analysis

All bulk rock isotopic measurements were performed in CRPG Nancy, using continuous acidification under helium flow. The methodology followed for the carbonate isotopic composition is described in Scheffer et al. (2016). The isotopic measurements were systematically doubled to check the homogeneity of the analyses. Isotopic compositions are quoted in the standard delta per mil notation (‰) relative to the Vienna Pee Dee Belemnite (V-PDB) reference frame, for both carbon and oxygen. Carbon and oxygen isotope compositions of calcite and dolomite cements were determined by using an auto sampler Gasbench coupled to a Thermo Scientific MAT253 isotope ratio mass spectrometer (IRMS). About 250–300 µg of each carbonate sample were extracted using a Dremel tool (1 mm diameter sampling hole). The obtained powders were then reacted with 2 ml of supersaturated orthophosphoric acid at 70°C for at least 5 h in a He atmosphere. Ten measurement cycles of the produced CO_2 isotopic composition were performed with a Thermo-Scientific-MAT-253 continuous flow isotope ratio mass spectrometer. All sample measurements were adjusted to the internal reference calibrated on the international standards MCt, NAG7-RT, BR-516, BR-9107 and CA10-8. The analytical precision for the isotopic measurements is ±0.02‰.

For the *in situ* carbon and oxygen isotopic analyses the instrument used was a Cameca IMS 1270 ion probe at CRPG (Nancy), using an in house dolomite standard (G119). When analyzing mixed dolomite-siderite phases, the same dolomite standard was considered. The thin sections were gold coated before mounting. During the analysis, the dolomite cements were sputtered with a Cs^+ beam source of 2-3 nA intensity inside a vacuum chamber, with 10 kV acceleration voltage. The analytical error for the *in situ* isotopic measurements is <0.67‰. Each spot analysis was performed under 40 cycles of 5 s each. The results were first reported as per mil deviations from the international standard SMOW (Standard Mean Ocean Water) with respect to $\delta^{18}O$ and in V-PDB for $\delta^{13}C$.

For consistency and to compare with the bulk rock values, the oxygen values were converted to PDB based on the following formula: $\{\delta^{18}O_{V\text{-}SMOW}=1.03086*\delta^{18}O_{V\text{-}PDB}+30.86\}$ after

Friedman and O'Neil (1977); Kendall and Caldwell (1998); Hoefs (2009); Zhao and Zheng (2013).

2.7 Micro X-Ray Fluorescence

Micro-XRF maps were obtained using a Bruker-Nano M4 Tornado instrument in SCEM, GeoRessources Nancy. This system has a Rh X-ray tube with a Be side window and polycapillary optics giving an x-ray beam with a diameter of 25-30 µm on the sample. The X-ray tube was operated at 50 kV and 200 µA. X-rays were detected by a 30 mm^2 xflash® SDD with an energy resolution of <135 eV at 250,000 cps. All analyses were carried out at 2 kPa vacuum. Main elements such as Ca, Mg, Mn, Fe, Ti, Al, K, Na and Si were mapped and composite chemical images were generated.

2.8 X-ray Diffraction (XRD)

The mineralogical analyses were performed on bulk rock powder of carbonate cemented sandstones and on oriented clay extracts using a Bruker D2 Phaser equipped with a LynxEye XE-T detector, available at GeoRessources. The interpretation software package used for the evaluation of the diffractograms was Diffrac.Suite along with EVA. The analysis was repeated twice, first before (air-dried) and then after ethylene-glycol treatment, since swelling clays were identified.

3 Results from Sedimentology, Petrography and bulk-rock Geochemistry

3.1 Description

Sediments, such as clays, silts and sands, most of the times grain supported as well as a few consolidated facies represented by dolomite cemented and by matrix (clay) supported sandstones represent the facies recognized in the Zoovch Ovoo depocenter. With respect to

the dolomite cemented facies, the sandstones can have various grain sizes from fine to very coarse. The sandstones are mostly composed of quartz (40 to 80%), feldspars as K-feldspars (microcline, orthoclase, some % to 25%) and plagioclases (5 to 20%), minor phases (apatite, ilmenite) and a few accessories of magmatic origin (monazite, zircon, xenotime, apatite, ilmenite, rutile, and anatase). On average, dolomite cement accounts for 30% of the sandstone by volume (calculated on bulk rock analysis). The clay/phyllosilicate fraction (biotite, chlorite, muscovite in the coarse grained fraction) was not abundant and not systematically present. The predominant clay fraction is smectite, on the basis of X-Ray diffraction analysis. The typical swelling of smectite was recognized at 14-17 Å. Kaolinite is the second more abundant clay mineral.

According to the sedimentological study (Parize et al., 2013) in the roll-front area there are two discrete lithological units. The first unit is composed of finely laminated to stratified homolithic to heterolithic silty to sandy-clay. These fine sediments correspond to varves and compose the background (annual) sedimentation. The second unit is very coarse, sandy to (micro)conglomeretic, most of the times homolithic, with granules of intraclasts originating from the fine unit. The coarse sediments correspond for most of their part to sudden flow episodes.

Using whole rock geochemistry for every lithology recognized in the Zoovch Ovoo reservoir i.e. sand, claystone, siltstone and dolomite cemented sandstone, a diagram of Ca (at%) versus Mg (at%) was used (**Figure 5**). The results from the *in situ* analysis of dolomite cements (data from EPMA; **Table 1**) were also cross-plotted on the same diagram. Most of cemented sandstones lie close to lines defined by dolomite stoichiometry (pure dolomite or Zoovch Ovoo dolomite). The zoomed version of the diagram suggests that many of the whole rock sand, siltstone and claystone samples contain a few percent of dolomite cement as they plot close to the same dolomite trendlines. A few siltstone and claystone lithologies show an enrichment in Mg linked to the presence of Mg-rich phyllosilicates.

However, dolomite cements from the Zoovch Ovoo cemented sandstones deviate from the ideal dolomite stoichiometry line (Ca/Mg=1). Instead they follow a stoichiometry that is similar

to the average value of the dolomite crystals measured by EPMA (Ca/Mg=1.495±0.1). Thus, dolomite is Ca enriched, hence Mg depleted and Ca and Mg are both partially substituted by Fe and Mn (**Table 1**) as shown in the following section.

3.2 Dolomite cements typology

It was necessary to understand if the different dolomite cements were genetically related and then construct their paragenetic succession. Hence, a dolomite classification scheme, according to Sibley and Gregg (1987) and Scholle and Ulmer-Scholle (2003), was adopted in this study, primarily based on the optical properties of the carbonate minerals. Initially the dolomite fabrics were divided in two groups regarding the crystal boundaries; those with planar geometry (idiotopic) and those with non-planar (xenotopic). Then they were grouped according to their crystal size distributions which can be unimodal or polymodal. Finally, the carbonate minerals were classified based on their degree of preservation that indicates the resemblance of precursor allochem fabrics. It was concluded that the dolomite textures identified during the study of the Zoovch Ovoo sands can be summarized and classified into four categories. For simplicity reasons each type is referred by a number as presented in **Figure 6** and is discussed by order of paragenetic evolution.

3.2.1 Type I - Microcrystalline dolomite

The microcrystalline dolomite is extremely fine grained and usually consists of micron sized grains that can locally reach up to 10μm in size. The latter case considers individual crystals that may not be discriminated by ordinary microscopy. However, under cathodoluminescence they are unimodal with discrete crystal boundaries and early zoning, allowing a distinction from the main microcrystalline mass, which is dull-red and has no geometry. The microcrystalline fabric can be found either as cement, filling the intergranular porosity or as dispersed patches (spherular aggregates). In the first case the microcrystalline dolomite fully occupies the

intergranular porosity, binding the sand grains which are not in contact with each other (floating grains). In the second case, the relationships with the neighboring polymodal dolomite fabrics suggest gradual replacement processes. The size of each patch can be larger than 0.5mm. Very often the patches can be associated to a siderite phase (**Figure 7**). The microcrystalline cement has the potential of penetrating through the fractures of detrital grains. Petrography suggests that this is the earliest dolomite type. It was recognized in samples whatever their position within or outside the roll-front systems. (For interpretation of the references to colour in this figure legend, the reader is referred to the web version of this article).

3.2.2 Type II - Euhedral dolomite (planar-e)

Concerning the microcrystalline dolomite, the planar-e fabric may come as replacement fabric but it also occurs as filling of intergranular space. It consists of well-expressed equant rhombohedra with sharp crystal boundaries and dark nuclei, due to the presence of siderite cores. Most of the times they are unimodal and have a maximum thickness of 50μm, with siderite cores having an average of 25μm. The euhedral crystals can overgrow to form poecilitic texture by adding further syntaxial cement (**Figure 8**). The poecilitic crystals can reach up to 100μm in size and show perfect interlocking, significantly decreasing the intergranular porosity. The poecilitic crystals are characterized by slight changes in mean "Z" on BSE images at a few μm scale (possibly reflecting slow process of crystallization with oscillatory changes in water chemistry for Mn and Fe). In some cases the poecilitic crystals can have siderite zonations, followed by further dolomite overgrowth. In this case, the zonations are on average 20 μm thick (**Figure 8**). Under cathodoluminescence, the euhedral dolomite has dull-orange to dull-red colour while the poecilitic overgrowth is more shifted towards the dull-orange.

Although both varieties, (the planar-e and the overgrowth) have euhedral crystal geometry and are characterized by inclusional zoning, they are remarkably different under cross-polarized light. The early type has darker color and is expressed by well-developed sharp crystal faces. The poecilitic texture is brighter (probably due the higher concentration of Fe and

Mn) and very blocky/massive under cross-polarized light. The type II dolomite can be found on both sides of the roll-front, oxidized, reduced as well as outside the roll-front systems.

3.2.3 Type III - Subhedral dolomite (planar-s)

The planar-s fabric resembles the previous two types with the difference that the crystal boundaries are more irregular. The term subhedral is used when there is at least one planar surface left on the rhombohedral crystal, while the remaining are compromised. It is undifferentiated and massive under polarized light, with birefringence colours of higher order and has stronger red-orange colors under cathodoluminescence, compared to the precursors. The crystals are polymodal but still well connected, hardly leaving any porosity. The rhombohedral structures with their zonations although still present, are less discrete and have uncertain boundaries, with 50μm maximum size. Locally, there is evidence for recrystallization highlighted by even brighter yellow spots inside the subhedral fabric. The subhedral fabric is only present in samples that are directly associated to the roll-front.

3.2.4 Type IV - Anhedral dolomite (non-planar)

The anhedral fabric consists of densely packed undeveloped unzoned crystals with irregular crystal boundaries. Under cross-polarized light the dolomite crystals are very different from the other types, having a kind of pseudo-cleavage that resembles that of calcite. It is very massive and usually there are no evidences of individual crystals forming the dolomite cement. The dolomite cemented sandstones that contain the anhedral dolomite are characterized by increased intergranular porosity compared to the previous dolomite types. Under cathodoluminescence, the anhedral fabric has bright orange colour. It is undeveloped and has irregular boundaries. It shows no sign of zoning or earlier fabric. On the SEM images, it is clear that the anhedral dolomite post-dates the other interstitial phases (previous dolomite types,

sulfides, authigenic quartz). Thus, very possibly this type is the latest diagenetic. The type IV dolomite is present in samples irrelevant of their position to the roll-front.

3.2.5 Calcite (Outcrop samples)

The calcite textures identified can be generalized in two categories. The first is sparite cement that can contain sand grains. Sparite crystals have birefringence colors of higher order. The second referred as micrite (crystals smaller than 4 μm) has birefringence colors of lower order. It is found as binding sand grains or as calcite concretions void of detrital elements. These micrite samples contain a secondary calcite variety with sparite crystals, as veinlets. Furthermore, iron hydroxides were found associated to calcite crystals that show a clear zonation under cathodoluminescence.

3.3 Crystal chemistry and geochemical data

EPMA analyses confirmed the predominance of dolomite and in some rare occurrences of siderite, in the Sainshand Formation sediments, whereas calcite is restricted to the outcrops of the Bayanshiree Formation (**Figure 9** and **Table 1**). As already mentioned, a significant number of data points are shifted to the calcite end-member as they contain an excess of Ca by an average of 5 at.% while many points are shifted towards Mg. In particular, the highest enrichment in Ca is attributed to the early dolomite, namely the microcrystalline (Type I) which is shifted by 9 to 12 at.%, whereas the euhedral, subhedral and anhedral are more stoichiometric. Dolomite contains in addition a significant Fe and Mn contribution, ranging from 5 to 18 at.%. A few data points close to the siderite corner in **Figure 9**, represent the siderite phase associated with the microcrystalline (Type I) dolomite as well as the siderite cores and zonations associated with the euhedral (Type II) dolomite crystals.

The Sr versus Mn plot, inspired by Blamey et al. (2014) was used to illustrate the evolution pattern in trace elements along the dolomite paragenetic sequence and to compare the

different dolomite and calcite fabrics (**Figure 10** and **Table A1**). The Sr content is always lower than 600 ppm for dolomite and below 1000 ppm for calcite. There is a general evolution from the microcrystalline (Type I) dolomite and siderite, to the euhedral (Type II), the subhedral (Type III) and the anhedral (Type IV), by a gradual decrease of their Mn content, each time by approximately one order of magnitude. Meanwhile Sr decreases from about 200 ppm to around 60 ppm. Calcite concretions and micrite are characterized by higher Sr contents than dolomite, ranging from 200 to 600 ppm and Mn contents similar to those of dolomite ranging from 8.000-15.000 ppm. The calcite cements have the lowest Mn and Sr concentration compared to the other cements, with 200 to 6000 ppm and 50 to 160 ppm, respectively.

3.4 Rare Earth Elements

The REE spectra of the microcrystalline (Type I), the euhedral (Type II), the subhedral (Type III) and the anhedral (Type IV), as well as of the calcite fabrics (cement, micrite and concretion types) are presented in **Figure 11** and **Table A2**.

The different spectra of the type I dolomite presented in **Figure 11a**. Some diversity of the detailed petrography and REE geochemistry is noticed for type I dolomite. The spectra in the first case fluctuate from 0.4 to 0.5, in the second from 0.6 to 1 and in the third from 2.5 to 12, relative to the PAAS concentration. The bulk rock REE composition of the last two cases is also illustrated for comparison.

The spectra of the type II dolomite presented in **Figure 11b** indicate two different cases, the first for euhedral dolomite (single rhombohedra) and the second for poecilitic euhedral crystals. The REE distribution of the first is wider, fluctuating between 0.5 and 2 times the PAAS while enveloping the poecilitic crystals spectra that are narrowed between 1 and 1.8 times the PAAS. The bulk REE composition of the rocks that host these particular dolomite cements is also provided.

The spectra of the type III dolomite starts to be shifted towards the HREE and the REE concentration ranges between 0.18 and 0.5, while the spectra of type IV is even more shifted towards the HREE, and the REE concentration ranges between 0.12 and 0.5. The spectra of type IV dolomite are very mixed, locally with large variations for certain elements, i.e. for Ce, Eu, Tb and Yb.

In summary, type I to III dolomite are characterized by rather flat patterns, which are gradually depleted in REE from type I to type III (**Figure 11a, b, c**). There is also slight but progressive relative enrichment in HREE (Tb to Lu) from type I to III. The changes are more pronounced in type IV dolomite (**Figure 11d**), where the LREE are rather low and less than one time the PAAS concentrations, whereas the HREE are richer up to 8 times the PAAS concentrations. The type IV dolomite shows negative Eu anomalies in two cases. On the contrary in a single case the spectra returns negative Ce anomaly combined with strong positive Eu anomaly.

The calcite types display very flat REE spectra around 3 to 6 times the PAAS (**Figure 11e, f, g, h**). In particular the calcite cement (sparite) in sandstone (**Figure 11e**) returns a low to significantly negative Ce anomaly coupled to a medium positive Eu anomaly. The calcite concretions (**Figure 11f, g**) show slight positive Eu anomalies.

3.5 C, O stable isotopes of carbonates in dolomite and calcite cements

The stable isotope analyses for C and O were initially performed on whole rocks. The stable isotope compositions of the dolomite and calcite cements are provided in **Table 2** and are plotted on **Figure 12**. The dolomite cemented samples show a limited range for both isotopic systems. They yield $\delta^{18}O_{v\text{-}PDB}$ and $\delta^{13}C_{v\text{-}PDB}$ values ranging from -9.48 to -11.34 ‰ (mean -10.41‰) and from -5.59 to -7.71 ‰ (mean -6.65‰), respectively. In regard to the calcite samples the $\delta^{18}O_{v\text{-}PDB}$ and $\delta^{13}C_{v\text{-}PDB}$ values range from -11.68 to -14.56 ‰ (mean -13.12‰) and from -5.74 to -8.61 ‰ (mean -7.16‰), respectively. In addition there seems to be an inversely proportional geochemical trend between the dolomitic carbonate content and the

$\delta^{13}C$ v-$_{PDB}$ value of the dolomite cements. In general, the lowest the $\delta^{13}C$ v-$_{PDB}$ value, the highest the dolomitic carbonate content. Three groups may be distinguished. With about 40% carbonate content the $\delta^{13}C$ v-$_{PDB}$ value fluctuates from -7.71 to -6.15‰, with about 30% from -6.95 to -5.59‰ and with 20% from -6.70 to -5.78‰.

Due to the complexity of the dolomite cements, in situ isotopic analyses were performed on all four major dolomite fabrics, particularly focusing on the microcrystalline type I dolomite that was separated into three sub-categories according to petrography, namely i) the microcrystalline isolated grains (patches), (ii) the microcrystalline grains with siderite and (iii) the microcrystalline uniform cement (**Figure 13** and **Table 3**).

The *in situ* analyses for the $\delta^{18}O$v-$_{PDB}$ of the dolomite cements show very large dispersion and variability, in particular from -6.91 to -13.54‰ (end members). The microcrystalline type I fabric in all three cases studied (i) as grain/patch, (ii) as grain with siderite and (iii) as uniform cement, is clearly lighter than the next three dolomite cements with $\delta^{18}O_{V\text{-}PDB}$ values ranging from -8.49 to -13.54‰. The euhedral type II dolomite has $\delta^{18}O_{V\text{-}PDB}$ values between -6.91 to -11.87‰, the subhedral type III between -8.70 to -9.99‰ and finally the anhedral type IV between -7.89 to -12.64‰.

The *in situ* analyses for the $\delta^{13}C$v-$_{PDB}$ of the dolomite cements are as well within the envelope of the bulk rock measurements. Once more, the microcrystalline type I dolomite for all three occasions has a wider distribution with $\delta^{13}C$v-$_{PDB}$ ranging from -5.28 to -15.14‰, sometimes reaching -18.30‰. The microcrystalline patch type is always lighter than -8.00‰ while the microcrystalline uniform cement follows the opposite trend. The patch type with siderite is difficult to be analyzed by the ion-probe as the beam spot is of greater size than the mineral phases that are very closely related. Likewise, the euhedral type II dolomite ranges from -5.00 to 10.65‰, occasionally reaching -16.18‰ , the subhedral type III dolomite from -5.13 to 9.47‰ and finally the anhedral type IV dolomite from -5.59 to -7.71‰ , locally down to -17.20‰.

4 Discussion

4.1 Dolomite burial diagenesis

By considering Prost (2004) and Graham et al. (2001) it can be estimated that the maximum burial depth for the Sainshand formation was 500-600m. By taking into account basin modelling by Prost (2004) it may be deduced that the temperature of the formation did not exceed 30-35°C. According to Barker and Pawlewicz (1994), the mean random vitrinite reflectance of kerogen subjected to a maximum temperature of 62°C during burial could not exceed 0.40%. Vitrinite reflectance measurements in the Zoovch Ovoo sands led to %Rr=0.302±0.02 (Rallakis et al., 2019). Thus, it may be concluded that the highest temperature experienced by the dolomite cements can be estimated at about 40°C.

To place the different carbonate varieties into a genetic context, a paragenesis of the dolomite cements is proposed (**Table 4**). The following discussion of the paragenetic succession leads to document the relative chronology and geochemical evolution of the dolomite cements.

4.1.1 Possible origin of type I dolomite

The earliest dolomite determined in the paragenesis sequence (dolomite I) occurs as detrital grains or as cement in sandstones layers of limited vertical (up to a few decimeters) and lateral extension (no possible correlation between wells). When it appears as cement, it occupies the intergranular porosity of the sand grains which are not in contact with each other, indicating low compaction. This feature could hold the following genetic interpretations:

Kearsey et al. (2012) showed that primary microcrystalline dolomite may be formed during pedogenesis as a result of soil bacterial activity. An interplay between diagenesis and pedogenesis in an alluvial/lacustrine setting was presented by Pimentel (2001) to explain how the Mg/Ca ratio can increase progressively and ultimately lead to the dolomitization of pre-deposited pedogenic carbonates lead by two factors. First the concentration levels of Mg

increase if there is no available dissolved Si in the system, which would inhibit the formation of Mg-clays (e.g. palygorskite) and secondly the precipitation of calcite results in lower Ca levels; hence the percolating waters become progressively saturated in respect to dolomite. In the model of Díaz-Hernández et al. (2013) the partial dissolution of biological-derived pedogenic calcite was responsible for the formation of dolomite below the petrocalcic soil horizon. The dolomite formation was in part favored by the evapotranspiration processes of the soil and also by the presence of smectite that retained soil water, promoting Mg incorporation in the carbonate.

In the Zoovch-Ovoo area, dolomite I as detrital elements would then be linked to further erosion of pedogenetic layers and transportation before final deposition as rip-up-clasts (Taylor and Machent, 2011) together with other detrital sediments.

Another possibility for the origin of dolomite I as clast or as cement could be related to dolomite formation in surface evaporative systems. Indeed, Morrow (1982a) for instance proposes dolomite precipitation as a result of rapid chemical carbonate precipitation from a supersaturated (saline) solution shortly after deposition i.e. a few centimeters or meters of burial depth. According to Von der Borch and Jones (1976) and Morrow (1982b) microcrystalline patchy dolomite is often Ca enriched, extremely fine-grained (0.5 to 1µm), amorphous and forms spherular aggregates from direct precipitation in mixing zones of two fluids of different salinities. Such description is quite similar to the Zoovch Ovoo type I dolomite that forms 10 at.% Ca enriched spherular aggregates.

Dolomite I may then be a witness of very early cement formation in the sedimentary systems. This implies early Mg enrichment of surface waters. Worden and Burley (2003) described the progressive increase of the Mg/Ca ratio during meteoric water run-off on the surface, leading first to the formation of calcrete and then towards the terminal playa lake to dolocrete. Kuang et al. (2002) made a link between Ca^{2+} enrichment relative to Mg^{2+} in clays and climatic conditions. In their model the degree of aridity has a direct effect on Ca concentration as it has higher transfer ability than Mg due to its larger ionic radius (Sun et al.,

2015). Schmidt (1965) suggested that primary microcrystalline dolomite could be formed in similar environments but from an early replacement of aragonite mud before burial. Cojan (2010) and Casado et al. (2014) indicated that significant evaporation of a playa lake during semi-arid episodes causes the abruption of the main lake to smaller hypersaline ponds, where calcrete and dolocrete may be formed.

4.1.2 Interpretation of the presence of siderite

The intimate association of siderite and dolomite I suggests that they are co-genetic. The presence of siderite implies reducing conditions for Fe during early diagenesis. Such conditions may have been linked to bacterial activity (Coleman et al., 1993; Roh et al., 2003). The type II dolomite which follows dolomite I in the paragenetic sequence is as well associated to siderite indicating continued reducing conditions for iron in absence of reduced sulfur (i.e. bacterial sulfate reduction was not active). Alternating dolomite and siderite zonations in type II dolomite may then indicate fluctuating Eh conditions.

4.1.3 Successive episodes of dolomite cement formation

The type I dolomite cement presents the highest concentrations in Mn, while a decrease of several orders of magnitude is observed when considering the paragenetic succession, accompanied by a decrease in Sr to some extent. The REE's concentration follows a similar trend. The petrographic relationships as well as the decrease by some orders of magnitude in Mn and REE between dolomite types are expected for carbonate recrystallization (Blamey et al., 2014). Indeed, the same depletion pattern but for calcite cements deposited as well in fluvio-lacustrine settings is recorded in Blamey et al. (2014). The authors proved that late stage calcite that is sourced from a calcite precursor will be four times more depleted in REE and ten times more depleted in Mn during each cycle of dissolution and re-precipitation. Considering the trace elements content of the dolomite cements as well as literature, in the case of Zoovch

Ovoo it may be suggested that successive dolomite cements formation underwent at least four cycles of crystallization which is imprinted on their trace element and REE compositions. Such mechanism implies at least partial recycling of the initial dolomite (Type I) pool within cemented sandstone layers during progressive diagenesis. It may then be suggested that early sandstone cementation by dolomite could only occur within or nearby layers that recorded input of carbonate rip-up clasts during sedimentation. Localization of dolomite cemented sandstones within the Sainshand Formation would then be at least partially controlled by depositional conditions and eventually explain their distribution in space as layers of limited extension.

4.1.4 Burial diagenesis, roll-front events and uplift

Framboidal pyrite appears in the system only after the end of the poecilitic overgrowth, marking the onset of bacterial sulfate reduction (BSR) and eventually deeper burial. This may suggest that with on-going cementation, the bacterial community (i.e. mesophilic bacteria) switched from fermentation responsible for siderite formation, to sulfate reduction responsible for framboidal pyrite formation (Roh et al., 2003). In this case, during the overgrowth of type II dolomite (poecilitic texture), the diagenetic waters may have been reducing and have changed from sulfate poor (surface waters, siderite) to sulfate rich (brines, pyrite) with further burial. The poecilitic overgrowth type II dolomite is associated to framboidal pyrite concentric overgrowth which stands for a second pyrite generation, suggesting further burial and continuing reducing conditions.

In several cases, partial dolomite dissolution features, post-dating type II cement were documented. This feature was only observed in part of the Sainshand formation where roll-fronts are localized. This is evidenced on a petrographic point of view by deposition of uranium minerals in the newly formed porosity (**Figure 8**). In sediments that are not leached by the roll-front waters, the type II dolomite does not show any dissolution features. All this information suggests the intrusion of a new water mass in disequilibrium with dolomite, transporting dissolved uranium (in oxidized state i.e. U^{VI}) and thus showing a higher oxidation state than

the Sainshand aquifer. Such events may be indicative of intrusion of surface derived waters and may sign the beginning of uplift conditions.

Furthermore, in the dolomite paragenetic succession, the dissolution is followed by subhedral type III dolomite formation characterized by further depletion in Mn and in REE. This dolomite cement generation may be considered as indicative of restoration to dolomite equilibrium condition for waters (background of the hydrological system) after roll-front episodes. The dissolution features as well as type III dolomite are not observed outside of the roll-front area.

The type IV (anhedral) cement post-dates all other dolomite cements and marks therefore the latest dolomitization event in the Zoovch Ovoo sub-basin. The type IV dolomite is present within and outside roll-front influenced sediments. It is always contained in medium to very coarse sandstones that have high porosity. Type IV dolomite may characterize equilibrium of diagenetic waters in regards to dolomite during the uplift until most recent times.

4.2 Geochemical conditions of dolomite cements and calcite formation.

4.2.1 Carbonates precipitation waters

The $\delta^{18}O_{V\text{-}PDB}$ isotope compositions of the dolomite and calcite in the sandstone samples are plotted on **Figure 12** for the bulk rock and on **Figure 13** for the in situ analysis. The bulk rock dolomite values show little variation, in particular the $\delta^{18}O_{V\text{-}PDB}$ values range from -9.48 to -11.79‰ and define a domain at the boundary between continental rainfall and lacustrine waters, while the absence of values close to zero indicates that the carbonates are clearly not marine sourced (Hofer et al., 2013). Furthermore the fact that the $\delta^{18}O_{V\text{-}PDB}$ data show no specific trend with the grain sizes of the sandstones indicates that the dolomite cements are not facies controlled.

The *in situ* $\delta^{18}O_{V\text{-}PDB}$ measurements on specific cements are characterized by values sometimes opposing to the bulk rock isotopic analyses. For the $\delta^{18}O_{V\text{-}PDB}$ the microcrystalline

dolomite I fabric is more depleted than the next three dolomite cements. The euhedral type appears in two groups, a lighter and a heavier. Since this type is directly evolving from type I, the lighter values might represent influence from type I. The overall lighter nature of type I probably suggests that it was formed in waters closer to the surface, a feature consistent with its suspected surface to subsurface origin as explained earlier. Other possible explanations could be lower temperature or slightly different waters. Consequently, the remaining three dolomite cement types crystallized at depth and as such they are in equilibrium with the aquifer waters, which should be slightly enriched in heavier in oxygen isotopes (Kanduč et al., 2014).

To estimate the $\delta^{18}O$ of the waters, the fractionation of oxygen isotope for dolomite-water and calcite-water were considered in two diagrams from Köster and Gilg (2015) for dolomite and from Barbier et al. (2016) for calcite (**Figure 14**). These diagrams make use of the oxygen isotope equilibrium values of carbonates and the water temperature during carbonate formation to calculate the oxygen isotope values of the water. Calcites which occur in the outcropping Bayanshiree Formation were considered as having not experienced a burial deeper than one hundred meters (Prost, 2004). The petrography of dolomite cements suggests on the contrary that they were formed from early sedimentation stages to maximum burial (500-600 m as discussed earlier) and uplift episodes of the basin.

The estimated $\delta^{18}O$ of the waters at the origin of dolomite ranges from -11.5 to -9.5‰ (mean value of -11.25±1.75‰). The $\delta^{18}O_{V\text{-}PDB}$ values of waters at the origin of the calcite cements were calculated to range from -13 to -11.5‰ (mean value of -12.25±0.75‰). As a conclusion, both dolomite and calcite were precipitated very probably from waters having $\delta^{18}O_{V\text{-}SMOW}$ values within the range of -10 to -12‰. These values, are similar even to those found for most present day waters in the Zuunbayan sub-basin, which according to measurements performed by Grizard (2017) are at the range of -9.29 to -11.45‰, indicative of continental rainfall, depleted in $\delta^{18}O$ due to the continental effect (Rayleigh fractionation). In addition, there is evidence that the East Asian climate during Late Cretaceous was characterized by seasonal monsoons and by tropical to sub-tropical arid and hot semi-desert and saliniferous lake districts with incoming

moisture from the West being blocked by the coastal mountains of East Asia (Chen et al., 2012). Conceivably, the similarity of oxygen isotopic waters in equilibrium with carbonates and todays aquifers may suggest that Rayleigh fractionation of the rain fall waters was similar i.e. the basin was located in intra-continental situation far from seashore.

4.2.2 The origin of carbon in dolomite and calcite cements

According to Wang et al. (2016) carbonates with $\delta^{13}C_{V\text{-}PDB}$ values ranging from -4 to 4 ‰ (PDB) are found in most marine carbonates with little influence of organic carbon. Therefore it could be suggested that the carbonates with $\delta^{13}C_{V\text{-}PDB}$ below -4 ‰ may indicate a moderate organic carbon influence. According to Suess and Whiticar (1989), values of $\delta^{13}C_{V\text{-}PDB}$ between -35.0 to -4.0 ‰ indicate organic carbon contribution, originating from the CO_2 that is released to the pore fluid due to decarboxylation of organic matter (i.e. bacterial fermentation). Decarboxylation of organic matter during shallow burial is possible as it is not necessarily linked to increasing temperatures (Irwin et al., 1977).

Alternatively, Fourcade et al. (2002) in their study on Paris basin proposed that most carbonates formed by sedimentary brines close to basement contain carbon directly recycled from traces of carbonates present in magmatic and metamorphic rocks. In such case, sedimentary carbonates have a $\delta^{13}C$ in between -8 and -12 ‰ (similar to that of disseminated carbonates in the basement) and were interpreted to be formed by metamorphic fluids in equilibrium with graphite in the basement and then redistributed in newly formed carbonates at several stages. Such disseminated carbonates can be present in the detrital grains and clasts of the Sainshand formation sands, which are all provided by erosion of magmatic or metamorphic basement rocks and may have been dissolved then by aquifer waters. The precipitated carbonate cements keep the initial value of the basement carbonates. Thus, the dissolution and recrystallization at constant temperature probably did not affect the $\delta^{13}C$ value, considering that there is no other carbonate pool contributing to the system (Sensula et al., 2006; Wang et al., 2016).

4.2.3 Conditions of calcite formation

Calcite has been exclusively found in outcropping samples while dolomite cements are solely present in deep core samples. Despite the fact that oxygen isotopes interpretation suggests that the water source for both carbonate cements is identical (continental rainfall), the strictly separation of calcite and dolomite cements indicates a strong difference in water chemistry between surface poor (Mg poor) and depth (Mg rich). In detail, the two groups of calcite cements are distinguished on the basis of Sr and Mn contents. Concretions and micrite are enriched in both Sr and Mn, while calcite cement is more depleted. According to Malone and Baker (1999) calcite precipitating at the upper few meters of the sedimentological column from supersaturated fluids will have elevated Sr content. On the contrary calcite that has been recrystallized via dissolution and recrystallization (increasing burial depth, temperature and time), will have lower Sr concentration. In the case of the studied samples, it could be deduced that the recrystallized calcite phases (Sr<350 ppm) are derived from Sr poor waters. Concretions and micrite (Sr above 350 ppm) are derived from Sr rich waters, which may reflect surface waters of much greater salinity. Some surface calcite cements show very low content of Ce. The mobility of Ce during dissolution processes depends on pH and Eh conditions during continental chemical weathering (Alfimova et al., 2011; Franchi et al., 2016). In oxidative settings Ce solubility is very low, resulting in aqueous solutions poor in this element. Carbonates precipitated from such waters thus present strong negative Ce anomaly. The oxidative character of the waters would be consistent with the low Mn that also characterizes these calcite cements. Calcite cement in the Bayanshiree Formation would therefore be formed by surface waters at shallow depths during Turonian and post-Turonian times, very probably reflecting calcrete conditions of formation (Haldar, 2018).

4.2.4 Geochemical conditions of dolomite formation

The weathering of the mafic rock outcrops (basalt) at the regional area is the strongest candidate for the Mg^{2+} source along with Fe^{2+} and Mn^{2+} (olivine, pyroxene), while the

abundance of nesosilicate (i.e. zircon) and phosphate (monazite, xenotime and apatite) minerals, present among the detrital elements, could be responsible for the elevated REE.

High Mg/Ca solution ratios, elevated salinities, high [CO_3^{2-}] and abundant organic matter, are between the most important physico-chemical factors for dolomite formation (Morrow, 1982a). The metabolic activity of both aerobic and anaerobic bacteria, i.e. methanogenic and sulfate-reducing, has been proven to promote dolomite formation. To sustain their metabolism, bacteria interact with organic matter and minerals, producing [NH_3] and [CO_2], increasing the alkalinity (pH>9) leading to high [CO_3^{2-}] (Slaughter and Hill, 1991; Al-Awadi et al., 2009). According to kinetic models the $MgCO_3$ complex is also abundant and can be easily incorporated into the growing dolomite under such conditions (Sanjuan and Girard, 1996).

In continental systems, the salinities needed for dolomite precipitation must be higher than 3 g/L (Hammer, 1986); Last, 1990) and this salinity level must be maintained during all cementation stages. According to recent measurements (Grizard, 2017) the salinity of the groundwater at the site of Zoovch Ovoo fluctuates between 1 and 8 g/l and can exceptionally reach up to 20 g/l. The salinity of the formation fluids is accredited to the presence of Mg, Fe, Mn, Li and other cations that promote dolomite precipitation (Carpenter, 1980; Gaines, 1980) by substituting Ca (Morrow, 1982a). The high Fe and Mn concentrations in dolomite could be attributed to the interaction of the formation fluids with non-carbonate phases, such as siliciclastic sediments and Fe-rich clay minerals (Banner et al., 1988; Sena et al., 2014).

4.2.5 Roll-front and uranium mineralization

The microcrystalline, euhedral and anhedral dolomite cements (types I, II and IV) were recognized in both the reduced and oxidized areas of the roll-front. Exception is the subhedral type III dolomite which formation is a result of fluid-rock interactions between the roll-front waters and type I and II dolomite cements. Type III is thus the only dolomite cement controlled by the roll-front. Also, partial dissolution of euhedral dolomite II is a feature that has been linked to roll-front waters. Hence, it is possible that inside the mineralization zone dolomite layers

have been completely dissolved. Whether diagenetic dolomite will be transformed to type III or will be complete dissolved is probably a factor of the volume of the oxidizing waters and interaction time.

As a consequence, Type III cement is rare in comparison to the other dolomite cements occurrences. It therefore reinforces the idea that dolomite cement formation in the Sainshand formation is primarily controlled by burial diagenesis (**Figure 15**). So, dolomite cements can be considered as the best and rather unique geochemical indicators about paleofluid sources and formation conditions in these intracontinental series of unconsolidated sands.

5 Conclusion

Within the unconsolidated succession of the Sainshand Formation in the Zoovch Ovoo area, the scarce occurrence of dolomite cemented facies provided a unique opportunity to reconstruct a relative chronological succession from early to burial diagenesis conditions. They are also among the rare indicators available to documents fluid-rock interactions as most detrital minerals have remained unchanged since sedimentation.

The petrographical and geochemical study of cements in the Sainshand Formation of the Zoovch Ovoo area allowed to identify four dolomites types. The three of the four dolomite cement types, namely the type I, II and IV were recognized within all cemented sandstone layers. Conversely, dissolution features followed by type III dolomite were only recognized as linked to roll-front. As such, it was possible to build a scenario for dolomite evolution with type I probably being formed at initial depositional stages during early diagenetic conditions, followed by type II linked to burial diagenesis, type III linked to a change in water chemistry composition due to roll-front activity and finally type IV (post-diagenetic) linked to uplift. Considering published basin modelling, as well as vitrinite reflection measurements, it was estimated that the dolomite cement paragenesis does cover a burial history from surface to a maximum depth of 500-600m with a maximum temperature of 40°C.

By comparing stable isotope data obtained for both the Sainshand dolomite and calcite from the outcropping Bayanshiree Formation it was concluded that they were both precipitated from the same oxygen isotopic pool, namely meteoric water with significant differences in chemistry. The magnesium needed for increasing the Mg/Ca ratio of saline waters to allow precipitation of exclusively dolomite cements may be sourced from the erosion of the basic volcanic rocks of the regional outcrops, and the relative enrichment in Mg versus calcium may have also been favored by the surficial hydrogeologic conditions during sedimentation. An early diagenetic origin of dolomite is proposed for the dolomite cemented pebbles found in the lacustrine environments of Zoovch Ovoo. This early dolomite deposit acted then as the carbonate reservoir within the Sainshand formation, for further dolomite cements which were formed during the burial and uplift history through re-crystallization and/or dissolution-precipitation processes.

Supplementary data to this article can be found online at https://doi.org/10.1016/j.sedgeo.2020.105688.

Declaration of competing interest

The authors declare that they have no known competing financial interests or personal relationships that could have appeared to influence the work reported in this paper.

Acknowledgements

This work was performed and funded in the research framework between ORANO Mining and CREGU (*Centre de Recherches sur la Géologie des Matières Premières Minérales et Energétiques*), in the Laboratory of GeoRessources in Nancy, France (contract number 40077759 of 15/03/2016). We are grateful to COGEGOBI's geological team for the hospitality and the equipment provided during the field work as well as for taking care of the shipping of the samples from Mongolia to France. People from the laboratory of GeoRessources, in particular Marie Christine Boiron and Chantal Peiffert are acknowledged for their contribution

to the REE *in situ* analysis. Andreï Lecomte and Olivier Rouer are acknowledged for the crystal chemistry analyses and the manipulation of the analytical means. MicroXRF is an equipment co-funded by ICEEL (Carnot institute)-CREGU-Labex Resources 21 (reference ANR-10-LABX 21-LABEX RESSOURCES 21) and FEDER. A special thanks to Thomas Rigaudier and Nordine Bouden from the laboratory of CRPG in Nancy for their contribution towards the bulk-rock and *in situ* analysis of the C, O stable isotopes.

References

Al-Awadi, M., Clark, W.J., Moore, W.R., Herron, M., Zhang, T., Zhao, W., Hurley, N., Kho, D., Montaron, B. and Sadooni, F., 2009. Dolomite: Perspectives on a Perplexing Mineral. *Oilfield Review*, **21**, 32-45.

Alfimova, N.A., Felitsyn, S.B. and Matrenichev, V.A., 2011. Mobility of Cerium in the 2.8-2.1 Ga Exogenous Environments of the Baltic Shield: Data on Weathering Profiles and Sedimentary Carbonates. *Lithol. Miner. Resour.* **46**(5), 397-408.

Alonso-Zarza, A.M., Martín-Pérez, A., 2008. Dolomite in caves: Recent dolomite formation in oxic, non-sulfate environments. Castañar Cave, Spain. Sediment. Geol. 205 (3–4), 160–164. doi:10.1016/j.sedgeo.2008.02.006.

Banner, J.L., Hanson, G.N. and Meyers, W.J., 1988. Water-rock interaction history of regionally extensive dolomites of the Burlington-Keokuk Formation (Mississippian): isotopic evidence, In: Shuckla, V. and Baker, P.A., eds., Sedimentology and Geochemistry of Dolostones. *Society for Sedimentary Geology*, SEPM, Special Publication **43**, 97-113.

Barbier, M., Leprêtre, R., Callot, P.J., Gasparrini, M., Daniel, J.M., Hamon, Y., Lacombe, O. and Floquet, M., 2012. Impact of fracture stratigraphy on the paleo-hydrogeology of the Madison Limestone in two basement-involved folds in the Bighorn basin. (Wyoming, USA). *Tectonophysics*, **576-577**, 116-132.

Barker, C.E. and Pawlewicz, M.J., 1993. Calculation of Vitrinite Reflectance from thermal Histories and Peak Temperatures. A comparison of Methods. 216-229. In: Mukhopadhyay, P.K. and Wallace, G.D. (1994) Vitrinite Reflectance as a Maturity Parameter. Applications and Limitations. *ACS Symposium Series*, **570**, 294 p.

Boiron, M.C., Cathelineau, M., Richard, A., 2010. Fluid flows and metal deposition near basement/cover unconformity: lessons and analogies from Pb-Zn-F-Ba systems for the understanding of Proterozoic U deposits. *Geofluids*, **10**, 270-292.

Blamey, N.J.F., Azmy, K., Brand, U., 2014. Provenance and burial history of cement in sandstones of the Northbrook Formation (Carboniferous), western Newfoundland, Canada: a geochemical investigation. *Sediment.Geol.* **299**, 30-41.

Casado, A.I., Alonso-Zarza, A.M., La Iglesia, Á., 2014. Morphology and origin of dolomite in paleosols and lacustrine sequences. Examples from the Miocene of the Madrid Basin. *Sediment. Geol.* **312**, 50-62 (ISSN 0037-0738).

Carpenter, A.B., 1980. The chemistry of dolomite formation I: the stability of dolomite: in Zenger, D.H., Dunham, J.B. and Ethington, R.G. eds., Concepts and Models of Dolomitization: Society of Economic Paleontologists, *Mineral Special Publication*, **28**, 111-121.

Cheburkin, A. and Shotyk, W., 1996. An Energy-dispersive Miniprobe Multielement Analyzer (EMMA) for direct analysis of Pb and other trace elements in peats. *Fresenius Journal of Analytical Chemistry*, **354**, 688-91.

Chen, J., Zhao, P., Wang, C., Huang, Y., Cao, K., 2012. Modelling East Asian climate and impacts of atmospheric CO_2 concentration during the Late Cretaceous (66 Ma). *Paleogeography, Paleoclimatology, Palaeoecology*, **385**, 190-201.

Coleman, M.L., Hedrick, D.B., Lovley, D.R., White, D.C. and Pye, K., 1993. Reduction of Fe(III) in sediments by sulphate-reducing bacteria. *Letters to Nature*, **361**, 436-438.

Colson, J. and Cojan, I., 1996. Groundwater dolocretes in a lake marginal environment: an alternative model for dolocrete formation in continental settings (Danian of the Provence basin, France), *Sedimentology*, **43**, 175-188. doi:10.1111/j.1365-3091.1996.tb01466.x.

Cojan, I., 2010. Les évènements globaux au travers des plaines d'inondation ou le fil d'ariane des systèmes fluviatiles. Géologie appliquée. Université Pierre et Marie Curie-Paris VI. 93 pp.

Dahlkamp, F.J., 2009. Uranium Deposits of the World: Asia, Berlin Heidelberg: Springer-Verlag, 493 pp.

Díaz Hernández, J.L., Sánchez-Navas, A., Reyes, E., 2013. Isotopic evidence for dolomite formation in soils. Chem. Geol. 347, 20–33. doi:10.1016/j.chemgeo.2013.03.018.

Dott, R.H.Jr., 1964. Wacke, greywacke and matrix-what approach to immature sandstone classification? *J. Sediment. Petrol.* **34**(3), 625-632.

Fourcade, S., Michelot, J.L., Buschaert, S., Cathelineau, M., Freiberger, R., Coulibaly, Y., Aranyossy, J.F., 2002. Fluid transfers at the basement/cover interface part I. Subsurface recycling of trace carbonate from granitoid basement rocks (France). *Chem. Geol.* 192, 99-120.

Fowler, A.D., Doig, R., 1982. The significance of europium anomalies in the REE spectra of granites and pegmatites. GCA 47 (6), 1131–1137. doi:10.1016/0016-7037(83)90243-0.

Franchi, F., Turetta, C., Cavalazzi, B., Corami, F., Barbieri, R., 2016. Trace elements and REE geochemistry of Middle Devonian carbonate mounds (Maïder Basin, Eastern Anti-Atlas, Morocco): Implication for early diagenetic processes. *Sediment. Geol.* **343**, 56-71.

Friedman, I. and O'Neil, J.R., 1977. Compilation of stable isotope fraction factors of geochemical interest. In: Fleischer, M. (Ed), Data of Geochemistry. In: 440-1212 United States Geological Survey Professional Paper, sixth edition.

Gaines, A.M., 1980. Dolomitization kinetics: Recent experimental studies. SEPM Special Publication 28, 81–86. doi:10.2110/pec.80.28.0081.

Graham, S.A., Hendrix, M.S., Johnson, C.L., Badamgarav, D., Badarch G., Amory, J., Porter, M., Barsbold, R., Webb, L.E., and Hacker B.R., 2001. Sedimentary record and tectonic implications of Mesozoic rifting in Southeast Mongolia. *Geol. Soc. Am. Bull.* **113**, 1560–1579.

Grizard, P., 2017. Fonctionnement hydrogéologique et hydrochimique du bassin crétacé de Tsagaan Els (Dornogobi, Mongolie). Thèse de doctorat, PSL Research University, Paris, 371 pp.

Haldar, S.K., 2018. Exploration Geochemistry - Chapter 5, 85-101: in Mineral Exploration: Principles and Applications, Second edition, 378 pp, doi.org/10.1016/C2017-0-00902-3.

Hammer, U.T., 1986. Saline Lake Ecosystems of the World. Junk, Dordrecht, 616 pp.

Heumann, J.M., Johnson, L.C., Webb, L.E., Taylor, P.J., Jalbaa, U., Minjin, C., 2014. Total and left–lateral displacement across the East Gobi Fault Zone, southern Mongolia: Implications for timing and modes of polyphase intracontinental deformation. *Earth Planet. Sci. Lett.* **392**, 1-15.

Hoefs, J., 2009. Stable Isotope Geochemistry, 6th ed. Springer-Verlag, Heidelberg, Berlin, New York, 285 p.

Hofer, G., Wagreich, M., Spötl, C., Bojar, A.V.; Melinte-Dobrinescu, M.C.; Smit, J., 2013. Carbon, oxygen and strontium isotopes as a tool to decipher marine and non-marine environments: Implications from a case study of cyclic Upper Cretaceous sediments. Isotopic Studies in Cretaceous Research, **382**. Geological Society, Special Publications, London, pp. 123–140.

Humphrey, J.D., 2000. New Geochemical Mixing-Zone Dolomitization at Golden Grove, Barbados. *J. Sediment. Res.* **70**(5), 1160-1170.

Irwin, H., Curtis, C. and Coleman, M., 1977. Isotopic evidence for source of diagenetic carbonates formed during burial of organic-rich sediments. *Nature*, **267**, 20-213.

Itterbeeck, J.V., Horne, D.J., Bultynck, P., Vandenberghe, N., 2005. Stratigraphy and palaeoenvironment of the dinosaur-bearing Upper Cretaceous Iren Dabasu Formation, Inner Mongolia, People's Republic of China. *Cretac. Res.* ***26*** **(4)**, 699-725.

Johnson, C.L., 2004. Polyphase evolution of the East Gobi basin: sedimentary and structural records of Mesozoic-Cenozoic intraplate deformation in Mongolia*. Basin Res.* **16**, 79-99.

Johnson, C.L. and Ritts, B.D., 2012. Plate interior poly-phase basins. In: Busby, C. and Azor Perez, A. (2012). Tectonics of Sedimentary Basins: Recent Advances. Wiley, Hoboken, ISBN: 9781444347135, 567-582.

Kanduč, T., Grassa, F., McIntosh, J., Stibilj, V., Ulrich-Supovec, M., Suprovec, I., Jamnikar, S., 2014. A Geochemical and Stable Isotope Investigation of Groundwater/Surface-Water Interactions in the Velenje Basin, Slovenia. *Hydrogeology Journal*, 15 pp.

Kearsey, T., Twitchett, R.J. and Newell, A.J., 2012. The origin and significance of pedogenic dolomite from the Upper Permian of the South Urals of Russia. *Geol. Mag.* **149** (2), 291-307.

Kendall, C., Caldwell, E.A, 1998. Fundamentals of Isotope Geochemistry, In: Kendall, C., McDonnell, J.J., 1999. Isotope Tracers in Catchment Hydrology.. Els. Sci., 51–86. doi:10.1016/C2009-0-10239-8.

Köster, M.H. and Gilg, H.A., 2015. Pedogenic, palustrine and groundwater dolomite formation in non-marine bentonites (Bavaria, Germany). *Clay Miner.* **50** (2), 163-183.

Kuang, S.P., Xu, Z., Shang, S.S., Ma, Z.D., 2002. Applying geochemistry to research into Meso-Cenozoic climate: discussion on Jurassic climatic change in Sichuan Basin, China. Qingdao Institute of Chemical Technology. **3** (1), 4-9.

Lamb, M.A. and Badarch, G., 1997. Paleozoic sedimentary basins and volcanic-arc systems of southern Mongolia: New stratigraphic and sedimentologic constraints. *Int. Geol. Rev.* **39**, 542-576.

Last, W.M., 1990. Lacustrine dolomite—an overview of modern, Holocene, and Pleistocene occurrences. *Earth-Sci. Reviews*, **27**, 221-263.

Last, F.M., Last, W.M., Halden, N.M., 2010. Carbonate microbialites and hardgrounds from Manito Lake, an alkaline hypersaline lake in the north Great Plains of Canada. *Sediment Geol.*, **225**, 34-49.

Last, F.M., Last, W.M., Halden, N.M., 2012. Modern and late Holocene dolomite formation: Manito Lake, Saskatchewan, Canada. *Sediment. Geol.*, **281**, 222-237.

Leach, D.L., Sangster, D.F., Kelley, K.D., Large, R.R., Garven, G., Allen, C.R., Gutzmer, J., Walters, S., 2005. Sediment-hosted lead–zinc deposits: a global perspective. *Economic Geology*, 100th Anniversary volume, 261–607.

Le Goux, F., Banzragch, T.O., Delaunay A., Nyamdorj, B.I., Jaques, E., Korshunov, A., Parize, O. and Brouand, M., 2015. The Major Gobi Uranium Deposits, Upper Cretaceous East Gobi Basin, Mongolia: Geodynamical and Mineralogical Key Parameters of Uranium Ore Geology. In: Mineral Resources in a Sustainable World, 13th SGA Biennial Meeting 2015, **5**, 1815-1818.

Longerich H.P., Jackson S.E. and Günther D., 1996. Laser ablation inductively coupled plasma, mass spectrometric transient signal data acquisition and analyte concentration calculation. *J. Anal. At. Spectrom.* **11**, 899-904.

Malone, M.J. and Baker, P.A., 1999. Temperature dependence of the strontium distribution coefficient in calcite: an experimental study from 40° to 200°C and application to natural diagenetic calcites. *J. Sediment. Res.* **69** (1), 216-223.

Mather, C.C., Skrzypek, G., Dogramaci, S., Grierson, P.F., 2018. Paleoenvironmental and paleohydrochemical conditions of dolomite formation within a saline wetland in arid Northwest Australia. *Quaternary Science Reviews*, **185**, 172-188, doi:10.1016/j.quascirev.2018.02.007.

McLennan, S.M., 1989. Rare earth elements in sedimentary rocks: influence of provenance and sedimentary process. In: LIPIN, B.R., McKay, G.A. (Eds.), Geochemistry and Mineralogy of Rare Earth Elements, *Review of Mineralogy*, **21**. pp, 169-200.

Meyerhoff, A.A. and Meyer, R.F., 1987. Geology of heavy crude oil and natural bitumen in the USSR, Mongolia, and China. In: Meyer, R.F, ed., Exploration for heavy crude oil and natural bitumen: *AAPG Studies in Geology*, **25**, 31-101.

Morad, S., Al-Aasm, I.S., Ramseyer, K., Marfil, R. and Aldahan, A.A., 1990. Diagenesis of carbonate cements in Permo-Triassic sandstones from the Iberian Range, Spain: evidence from chemical composition and stable isotopes. *Sediment Geol.* **67**, 281-295.

Morrow, D.W., 1982a. Diagenesis 1. Dolomite – part 1: the chemistry of dolomitization and dolomite precipitation. *Geosci. Can.* **9** (1), 5-13.

Morrow, D.W., 1982b. Diagenesis 2. Dolomite – part 2: dolomitization models and ancient dolostones. *Geosci. Can.* **9** (2), 95-107.

Muchez, P., Heijlen, W., Banks, D., Blundell, D., Boni, M., Grandia, F., 2005. Extensional tectonics and the timing and formation of basin-hosted deposits in Europe. *Ore Geol. Rev.* **27**, 241–67.

Omer, M.F., Omer, D. and Zebari, B.G., 2014. High resolution cathodoluminescence spectroscopy of carbonate cementation in Khurmala Formation (Paleocene-L. Eocene) from Iraqi Kurdistan Region, Northern Iraq. *J. Afr. Earth Sci.* **100**, 243-258.

Parize, O., 2013. Le remplissage de la dépression de Tsagaan Els et les dépôts fluviatiles associés (Crétacé moyen, Bassin de Zuunbayan). Implication stratigraphiques et sédimentologiques sur le gisement de Zoovch Ovoo – Synthèse des résultats 2012-2013. Octobre 2013, édition décembre 2014. Rapport technique AMS-DGS-TEC-SDYRT-0008, (Poster AMS-DGS-TEC-SDY-RT-0008_PosterZoovchA1_2013).

Pearce, N.J.G., Perkins, W.K., Westgate, J.A., Gorton, M.P., Jackson, S.E., Neal, C.R. and Chenery, S.P., 1997. A compilation of new and published major and trace element data for

NIST SRM 610 and NIST SRM 612 glass reference materials. *Geostand. Geoanal. Res.* **21**, 101-114.

Pimentel, N.L.V., 2002. Pedogenic and early diagenetic processes in Palaeogene alluvial fan and lacustrine deposits from the Sado Basin (S Portugal). *Sediment. Geol.* **148**, 123-138

Prost, G.L., 2004. Tectonics and hydrocarbon systems of the East Gobi basin, Mongolia, AAPG Bull. **88** (4), 483-513.

Rallakis, D., Michels, R., Brouand, M., Parize, O., Cathelineau, M. (2019). The Role of Organic Matter on Uranium Precipitation in Zoovch Ovoo, Mongolia. *Minerals*, **9**, 310, doi.org/10.3390/min9050310.

Roberts, J.A., Bennett, P.C., Gonzalez, L.A., Macpherson, G.L. and Milliken, K.L., 2004. Microbial precipitation of dolomite in methanogenic groundwater. *Geol.* **32**, 277-280.

Roh, Y., Zhang, C.L., Vali, H., Lauf, R.J., Zhou, J. and Phelps, T.J., 2003. Biogeochemical and environmental factors in Fe biomineralization: magnetite and siderite formation. *Clay and Clay Minerals*, **51**(1), 83-95.

Rosen, M.R., Miser, D.E. and Warren, J.K., 1988. Sedimentology, mineralogy and isotopic analysis of Pellet Lake, Coorong region, South Australia, *Sedimentology*, **35**, 105-122.

Sánchez-Román, M., Vasconelos, C., Schmid, T., Dittrich, M., McKenzie, J.A., Zenobi, R. and Rivadeneyra, M.A., 2008. Aerobic microbial dolomite at the nanometer scale: Implications for the geologic record. *Geol.* **36**, 879-882. doi:https://doi.org/10.1130/G25013A.1.

Sanjuan, B. and Girard, H., 1996. Review of kinetic data on carbonate mineral precipitation. BRGM Report R39062, 91p.

Scheffer, C., Tarantola, A., Vanderhaeghe, O., Rigaudier, T., Photiades, A., 2016. CO_2 flow during orogenic gravitational collapse: Syntectonic decarbonation and fluid mixing at the ductile-brittle transition (Lavrion, Greece), *Chem. Geol.* **450**, 248-263.

Schmidt, V., 1965. Facies, diagenesis, and related reservoir properties in the Gigas Beds (Upper Jurassic), northwestern Germany: in Pray, L.C. and Murray, R.C., Dolomitization and Limestone Diagenesis, *Society of Economic Paleontologists*, Mineral Special Publication, **13**, 124-168.

Scholle, P.A. and Ulmer-Scholle, D.S., 2003. A color guide to the petrography of carbonate rocks: grains, textures, porosity, diagenesis, *AAPG Mem.* **77**, 474 pp.

Sena, C.M, John, C.M., Jourdan, A.L., Vandeginste, V.L. and Manning, C., 2014. Dolomitization of lower cretaceous Peritidal Carbonates by modified seawater: constraints from clumped isotopic paleothermometry, elemental chemistry, and strontium isotopes. *J. Sediment. Res.* **84**, 552-566.

Sensula, B., Boettger, T., Pazdur, A., Piotrowska, N. and Wagner, R., 2006. Carbon and oxygen isotope composition of organic matter and carbonates in recent lacustrine sediments. *Geochronometria*, **25**, 77-94.

Sibley, D.F., Gregg, J.M., 1987. Classification of dolomite rock textures. *J. Sediment. Res.* **57** (6), 967-975. doi:https://doi.org/10.1306/212F8CBA-2B24-11D7-8648000102C1865D.

Slaughter, M. and Hill, R.J., 1991. The influence of organic matter in organogenic dolomitization. *J Sediment. Petrol.* **61**, 296-303.

Spirakis, C.S., 1996. The roles of organic matter in the formation of uranium deposits in sedimentary rocks. *Ore Geol. Rev.* **11**, 53-69.

Spötl, C. and Wright, V.P., 1992. Groundwater dolocretes from the Upper Triassic of the Paris Basin, France: a case study of an arid, continental diagenetic facies. *Sedimentology*, **39**, 1119-1137.

Suess, E. and Whiticar, M.J., 1989. Methane-derived CO_2 in pore fluids expelled from the Oregon subduction zone. *Palaeogeogr. Palaeoclimatol. Palaeoecol.* **71**, 119-136.

Sun, G., Yin, J., Zhang, S., Lu, X., Zhang, S. and Shi, J., 2015. Diagenesis and sedimentary environment of Miocene series in Eboliang III area. *Environment. Earth Sci.* **74**, 5163-5179.

Taylor, K. and Machent, P.G., 2011. Extensive carbonate cementation of fluvial sandstones: An integrated outcrop and petrographic analysis from the Upper Cretaceous, Book Cliffs, Utah. *Mar. Pet. Geol.* **28** (8), 1461-1474.

Traynor, J.J and Sladen, C., 1995. Tectonic and stratigraphic evolution of the Mongolian People's Republic and its influence on hydrocarbon geology and potential. *Mar. Petrol. Geol.* **12**, 35-52.

Von der Borch, C.C and Jones, J. B., 1976. Spherular modern dolomite from the Coorong area, South Australia. *Sediment.* **23**, 587-591.

Wang, J., Cao, Y., Liu, K., Liu, J., Xue, X. and Xu, Q., 2016. Pore fluid evolution, distribution and water rock-interactions of carbonate cements in red-bed sandstone reservoirs in the Dongying Depression, China. *Mar. Pet. Geol.* **72**, 279-294.

Warren, J., 2000. Dolomite occurrence, evolution and economically important associations. *Earth Sci. Rev.* **52**, 1-81.

Wentworth, C.K., 1922. A scale of grade and class terms for clastic sediments. *J. Geol.* ***30***, 377-392.

Worden, R.H. and Burley, S.D., 2003. Sandstone Diagenesis: The Evolution of Sand to Stone, Sandstone Diagenesis: Recent and Ancient. *International Association of Sedimentologists*, 44 pp. ISBN: 978-405-10897-3.

Wright, D.T. and Wacey, D., 2005. Precipitation of dolomite using sulphate-reducing bacteria from Coorong Region, South Australia: significance and implications. *Sedimentology*, **52**, 987-1008.

Xie, X., Mingcai, Y., Wang, C., Li, L., Shen, H., 1989. Geochemical reference samples GSD 9-12, GSS 1-8, GSR 1-6, *Geostand. Geoanal. Res.* **13**, 83-179.

Zhao, Y.Y. and Zheng, Y.F., 2013. Geochemical constraints on the origin of post-depositional fluids in sedimentary carbonates of the Ediacaran system in South China. *Precambrian Res.* **224**, 341-363.

https://www.britannica.com/place/Mongolia. 2020. (Accessed 16 May 2020).

FIGURES

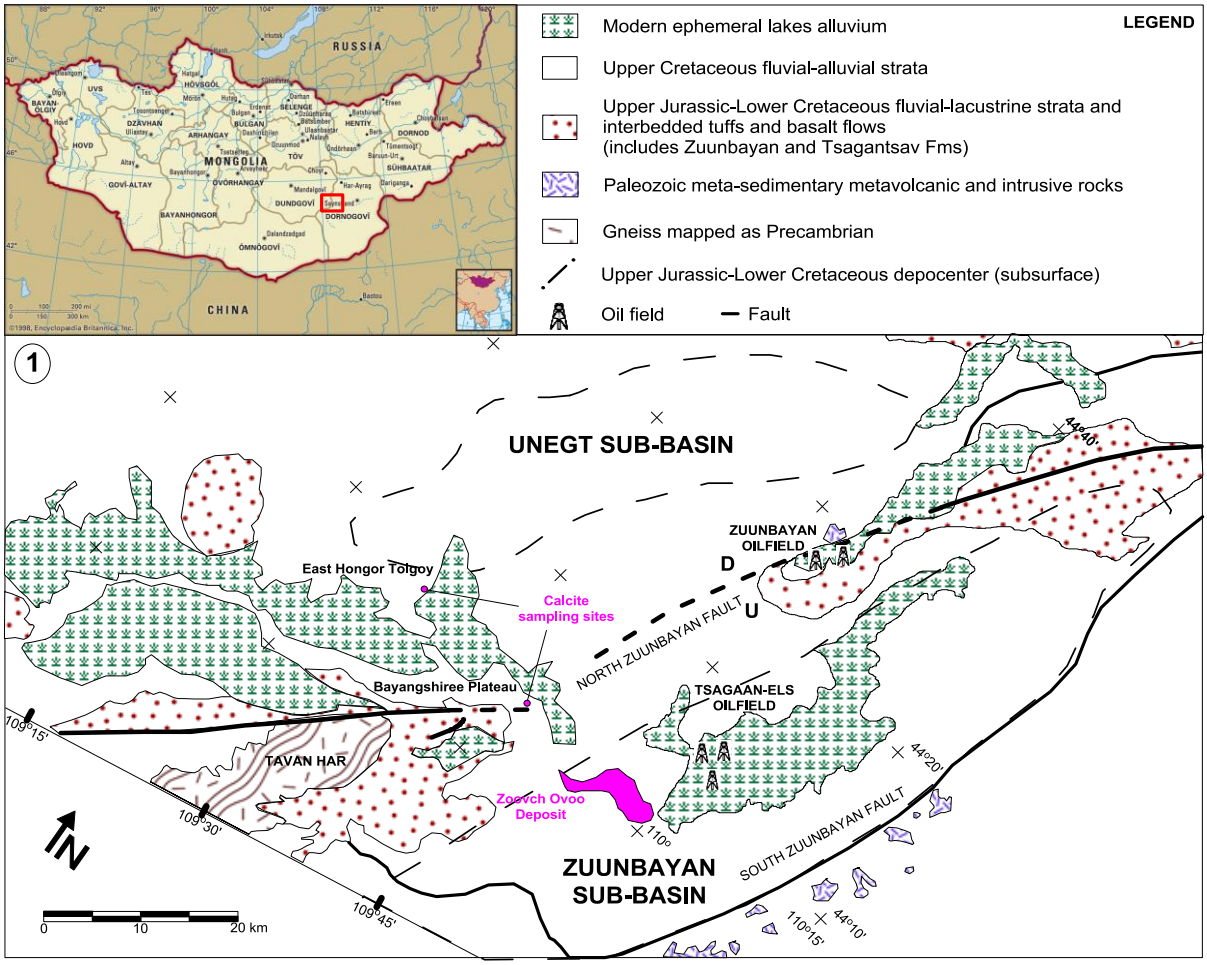
LEGEND
Modern ephemeral lakes alluvium
Upper Cretaceous fluvial-alluvial strata
Upper Jurassic-Lower Cretaceous fluvial-lacustrine strata and interbedded tuffs and basalt flows (includes Zuunbayan and Tsagantsav Fms)
Paleozoic meta-sedimentary metavolcanic and intrusive rocks
Gneiss mapped as Precambrian
Upper Jurassic-Lower Cretaceous depocenter (subsurface)
Oil field
Fault
RUSSIA
CHINA
MONGOLIA
1
UNEGT SUB-BASIN
ZUUNBAYAN OILFIELD
East Hongor Tolgoy
Calcite sampling sites
NORTH ZUUNBAYAN FAULT
D
U
Bayangshiree Plateau
TSAGAAN-ELS OILFIELD
TAVAN HAR
Zoovch Ovoo Deposit
SOUTH ZUUNBAYAN FAULT
ZUUNBAYAN SUB-BASIN
109°15'
109°30'
109°45'
110°
110°15'
44°40'
44°20'
44°10'
N
0
10
20 km

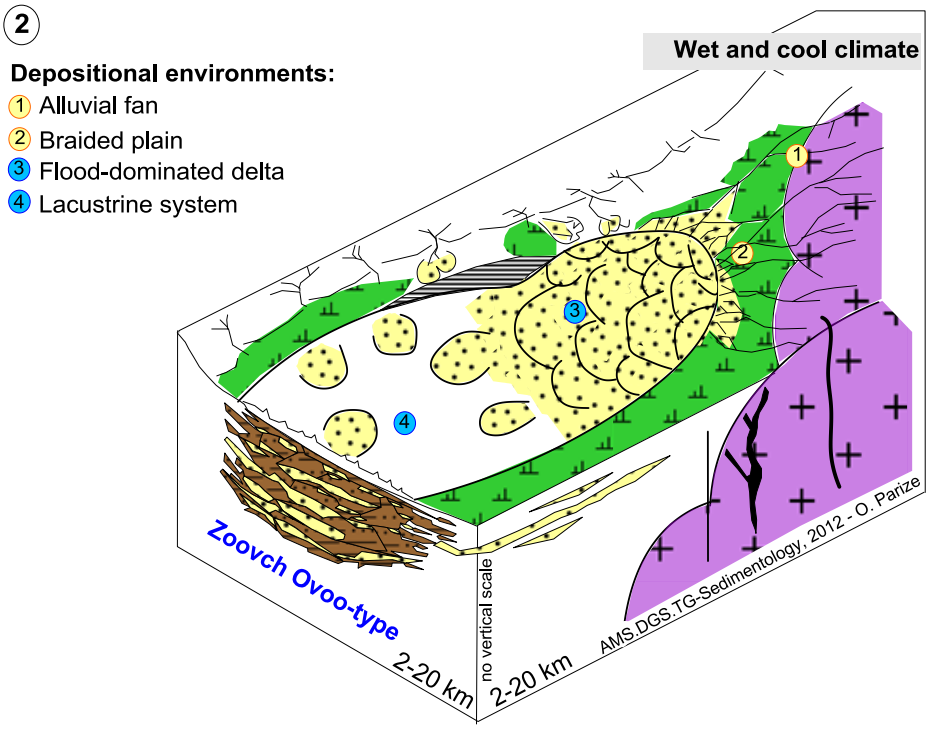
2
Depositional environments:
1 Alluvial fan
2 Braided plain
3 Flood-dominated delta
4 Lacustrine system
Wet and cool climate
Zoovch Ovoo-type
2-20 km
no vertical scale
2-20 km
AMS.DGS.TG-Sedimentology, 2012 - O. Parize

Figure 1: (1) Location map of Mongolia (Encyclopædia Britannica) highlighting the study area and simplified geological map of East Gobi Basin with the morpho-tectonic elements. The Zoovch Ovoo roll-front U deposit is located in the Zuunbayan sub-basin and the sampling sites of calcite in the vicinity of East Hongor Tolgoy and Bayanshiree plateau (map modified from Graham et al., 2001); (2) Depositional model of the Zoovch Ovoo depocenter in Cenomanian (modified from Le Goux et al., 2015).

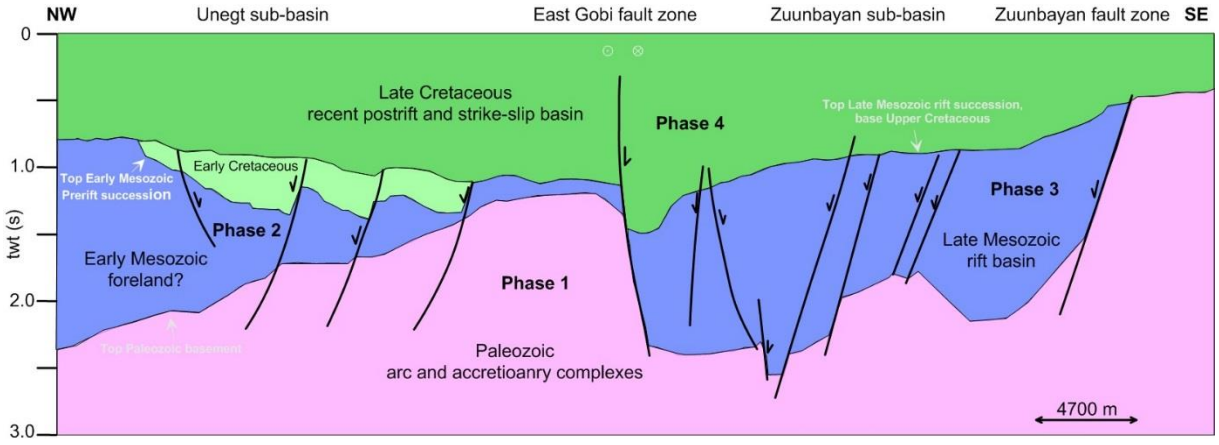

Figure 2: Seismic profile (in colour) across the East Gobi Basin featuring the four tectonic events that affected the development of the basin. The seismic profile is used to illustrate the Late Cretaceous sedimentary infill in Zuunbayan sub-basin. Note that the depth is measured in two-way-travel-time (modified from Johnson and Ritts, 2012).

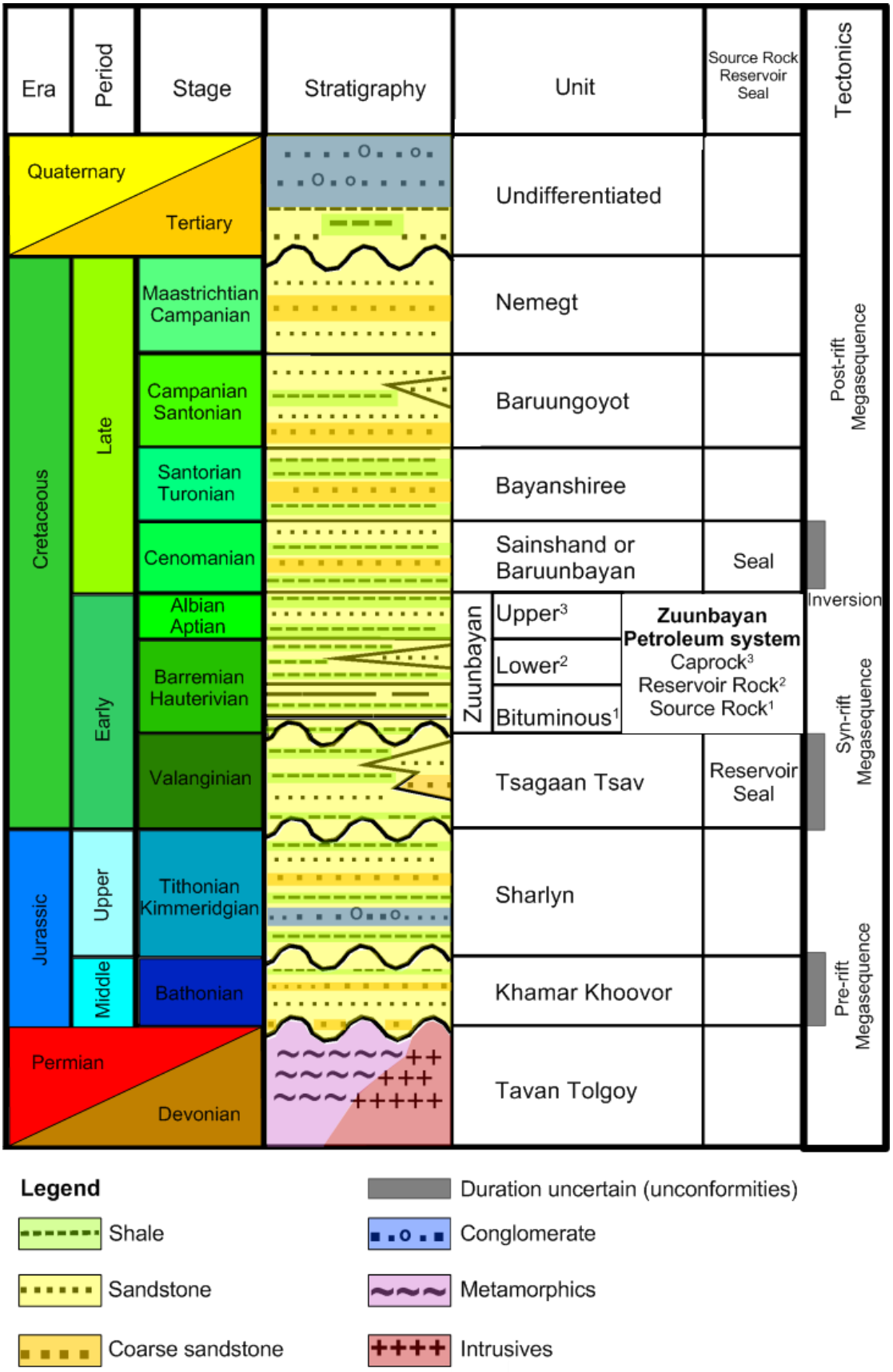
Era
Period
Stage
Stratigraphy
Unit
Source Rock
Reservoir
Seal
Tectonics
Quaternary
Tertiary
Undifferentiated
Cretaceous
Late
Maastrichtian
Campanian
Nemegt
Campanian
Santonian
Baruungoyot
Santorian
Turonian
Bayanshiree
Cenomanian
Sainshand or
Baruunbayan
Seal
Post-rift
Megasequence
Inversion
Albian
Aptian
Early
Barremian
Hauterivian
Zuunbayan
Upper3
Lower2
Bituminous1
Zuunbayan
Petroleum system
Caprock3
Reservoir Rock2
Source Rock1
Valanginian
Tsagaan Tsav
Reservoir
Seal
Syn-rift
Megasequence
Jurassic
Upper
Tithonian
Kimmeridgian
Sharlyn
Middle
Bathonian
Khamar Khoovor
Pre-rift
Megasequence
Permian
Devonian
Tavan Tolgoy
Legend
Shale
Sandstone
Coarse sandstone
Duration uncertain (unconformities)
Conglomerate
Metamorphics
Intrusives

Figure 3: Lithostratigraphical column of the East Gobi Basin including potential unconformities and tectonic episodes. Modified from Prost (2004).

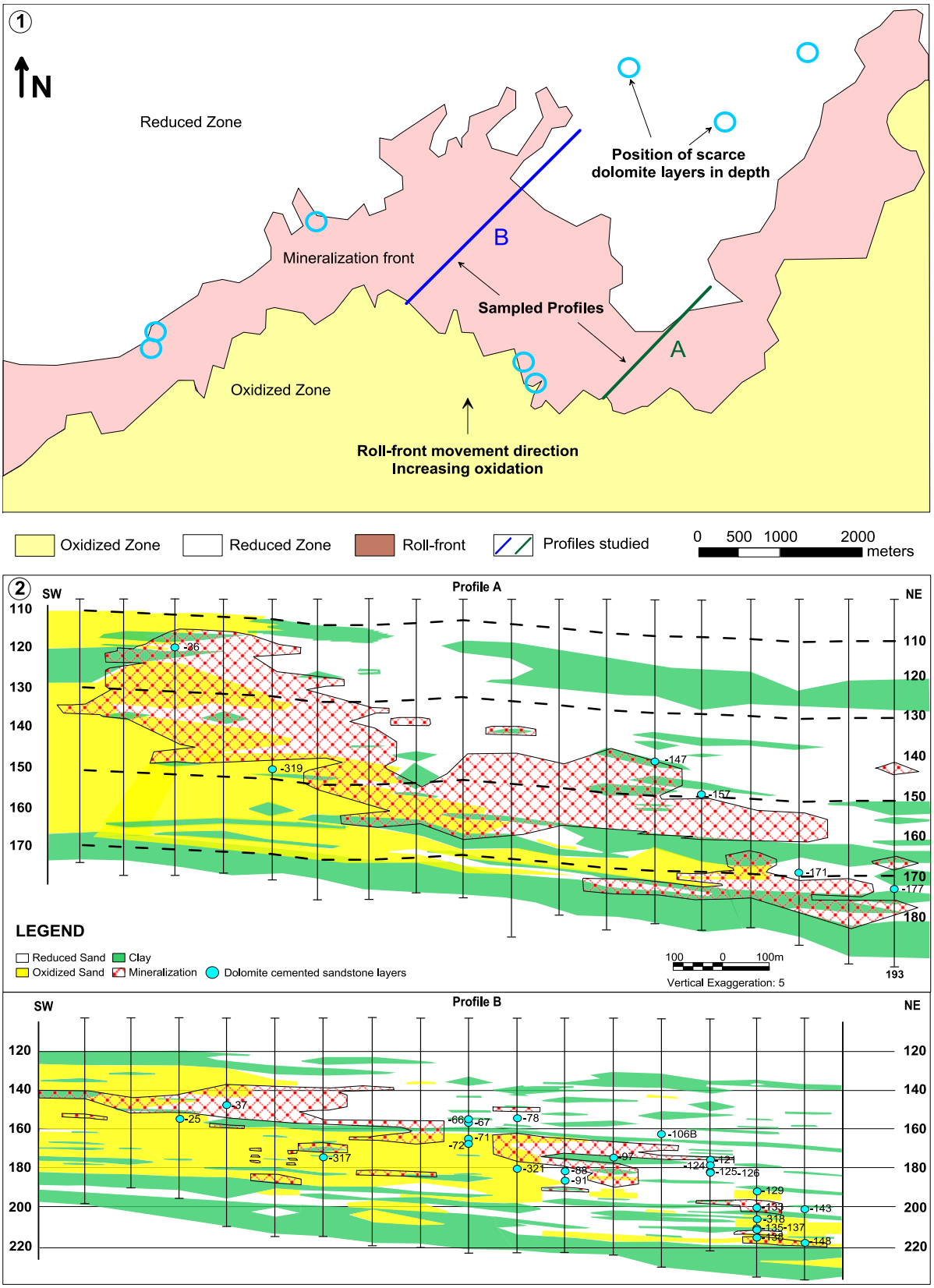

Figure 4: 1) Graphical representation of the Zoovch Ovoo roll-front in planar-view (simplified). Location of the two studied A in green and B in blue, respectively, as well as position of other scarce dolomite layers in depth from the mineralized area (roll-front) but also the reduced area (reduced zone). 2) Distribution of all sampled dolomite rich layers (blue circles) along profiles A and B: vertical lines represent wells, colors correspond to lithology (sands and clay rich layers) and red zones to the main U-ore roll-front. (For interpretation of the references to colour in this figure legend, the reader is referred to the web version of this article).

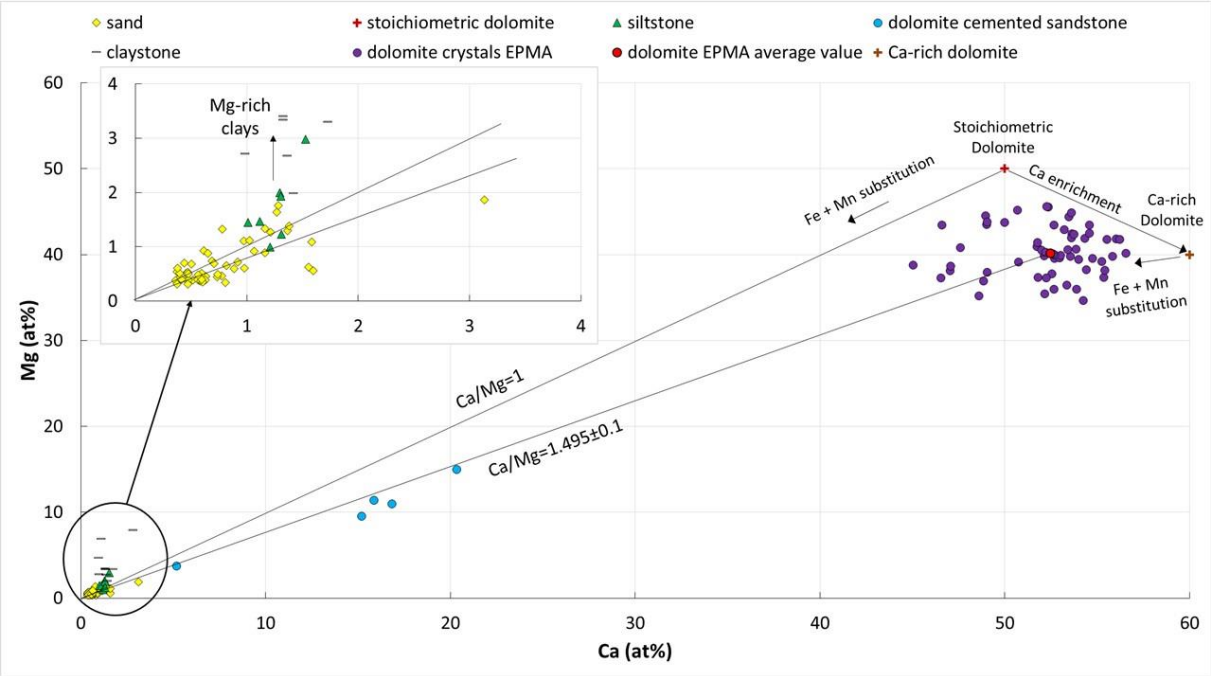

Figure 5: Ca versus Mg (at.%) diagram used to distinguish the dolomite cemented sandstone samples from the unconsolidated facies. Sand (yellow rhombs), claystone (black dash), siltstone (green triangles) and carbonate cemented sandstone (teal dots) samples were analyzed as whole rock by ICP-MS and are plotted at the left part of the diagram. Dolomite crystals (violet dots) were analyzed by EPMA and are plotted at the right part of the diagram. Zoomed version for the sand, claystone and siltstone samples is provided on the top left part of the diagram. Pure dolomite stoichiometry (red cross) is provided as a guideline, as well as the Ca-rich dolomite (brown cross). The average value of the dolomite crystals measured by microprobe (violet dots) is also indicated. (For interpretation of the references to colour in this figure legend, the reader is referred to the web version of this article).

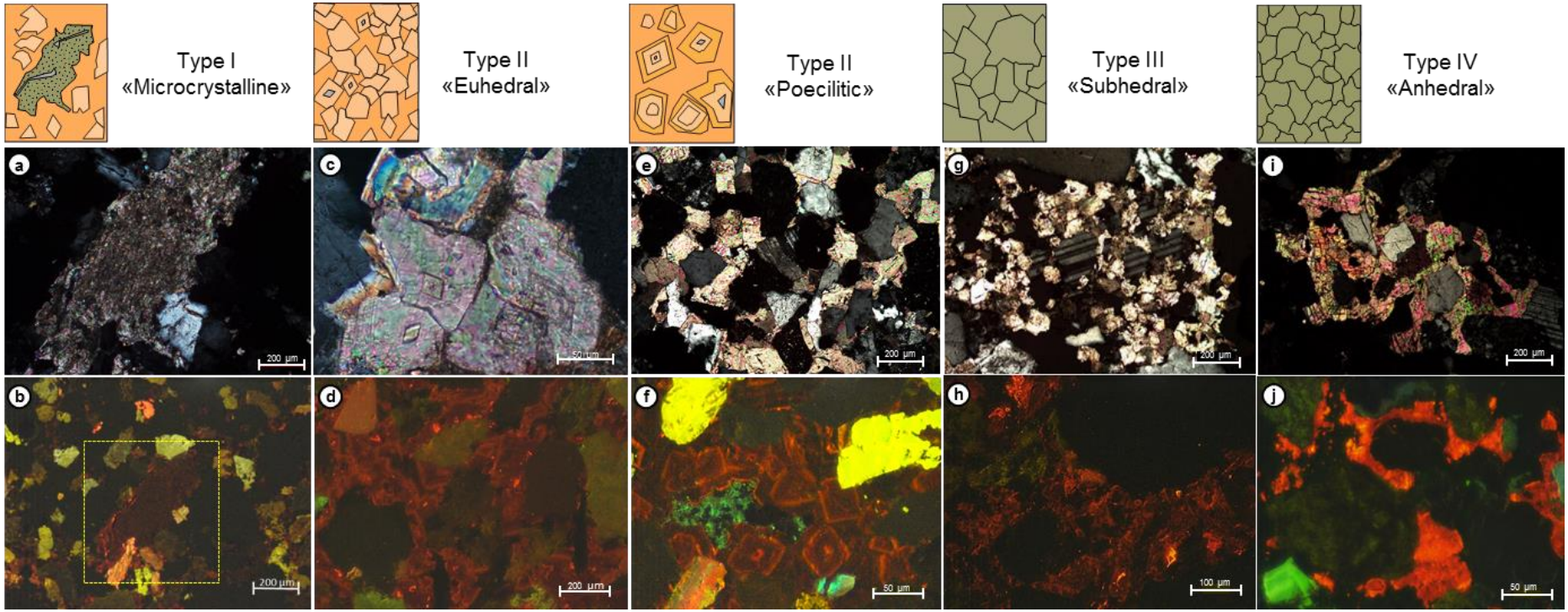

Figure 6: Optical photomicrographs under polarized/analyzed light (top) and cathodoluminescence (bottom). Typology is based on Sibley and Gregg (1987) and Scholle and Ulmer-Scholle (2003). (a, b) The microcrystalline fabric is found as uniform cement or as patches and may locally contain siderite; (c, d) The rhombohedral crystals of the euhedral fabric can evolve into large poecilitic crystals by accumulating syntaxial cement and they can locally have siderite cores/zonations (e, f); (g, h) The subhedral fabric stands for the partial dissolution/recrystallization of the previous two fabrics due to fluid-rock interaction episodes; (i, j) Finally the anhedral fabric is a uniform cement where individual crystals are not distinguishable.

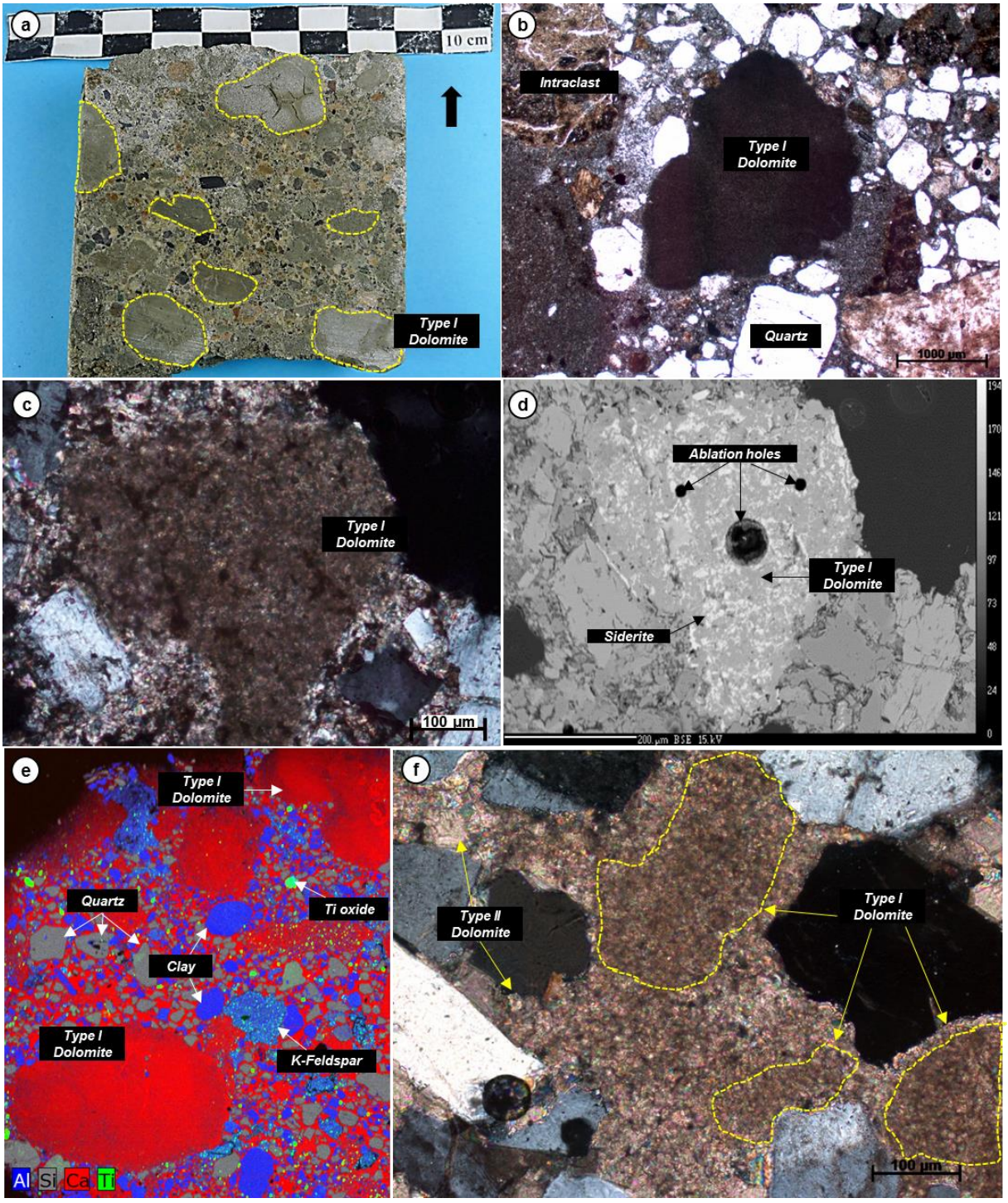

Figure 7: The petrographic characteristics of the microcrystalline type I dolomite. a) Macroscopic photograph of a dolomite cemented sandstone in reduced state containing microcrystalline dolomite grains/patches enclosed in yellow dashed lines. The black arrow marks the top of the well; b) Microcrystalline patch void of sand grains under plain light; c) Microcrystalline patch containing siderite under polarized/analyzed light; d) the same association as in (c) under back scattered electron mode. The siderite phase is clearly

discriminated; e) X-Ray microfluorescence map for Al (blue), Si (grey), Ca (red) and Ti (green) of a sandstone cemented by microcrystalline cement (binding phase in red), containing clasts of microcrystalline dolomite void of sand grains (red), as well as clay intraclasts (blue), silicates (grey) and titanium oxides (green); f) Sandstone cemented by microcrystalline type I and euhedral type II dolomite. The sand grains are not in contact with each other (floating grains). (For interpretation of the references to colour in this figure legend, the reader is referred to the web version of this article).

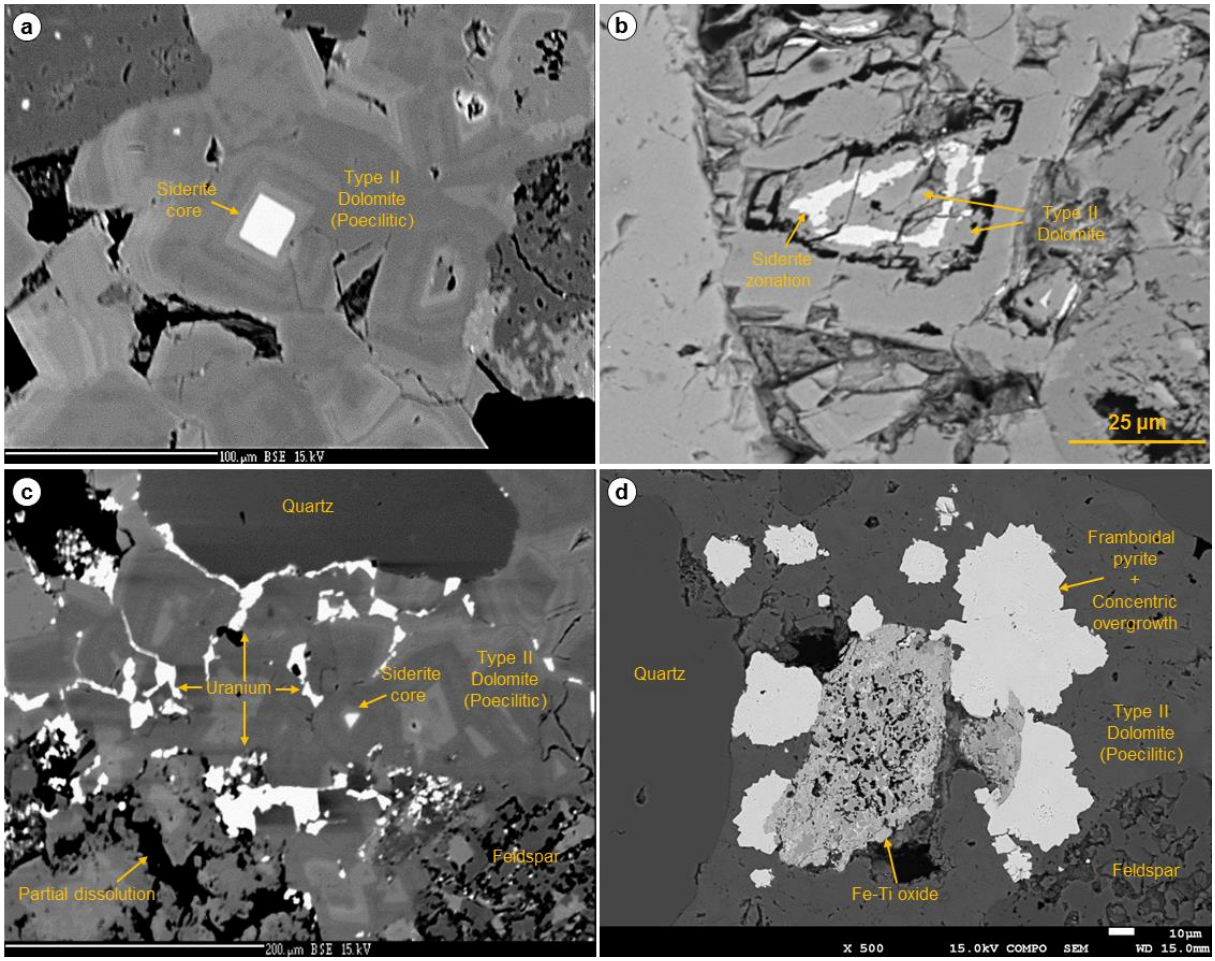

Figure 8: The petrographic characteristics of the euhedral type II dolomite under SEM-BSE. a) Poecilitic texture containing siderite core; b) siderite zonation of a euhedral dolomite crystal; c) uranium cement precipitating in the intergranular porosity around poecilitic dolomite crystals. Partial dissolution features of the dolomite are observed; d) framboidal pyrite with concentric overgrowth growing around an Fe-Ti oxide, encompassed by poecilitic dolomite.

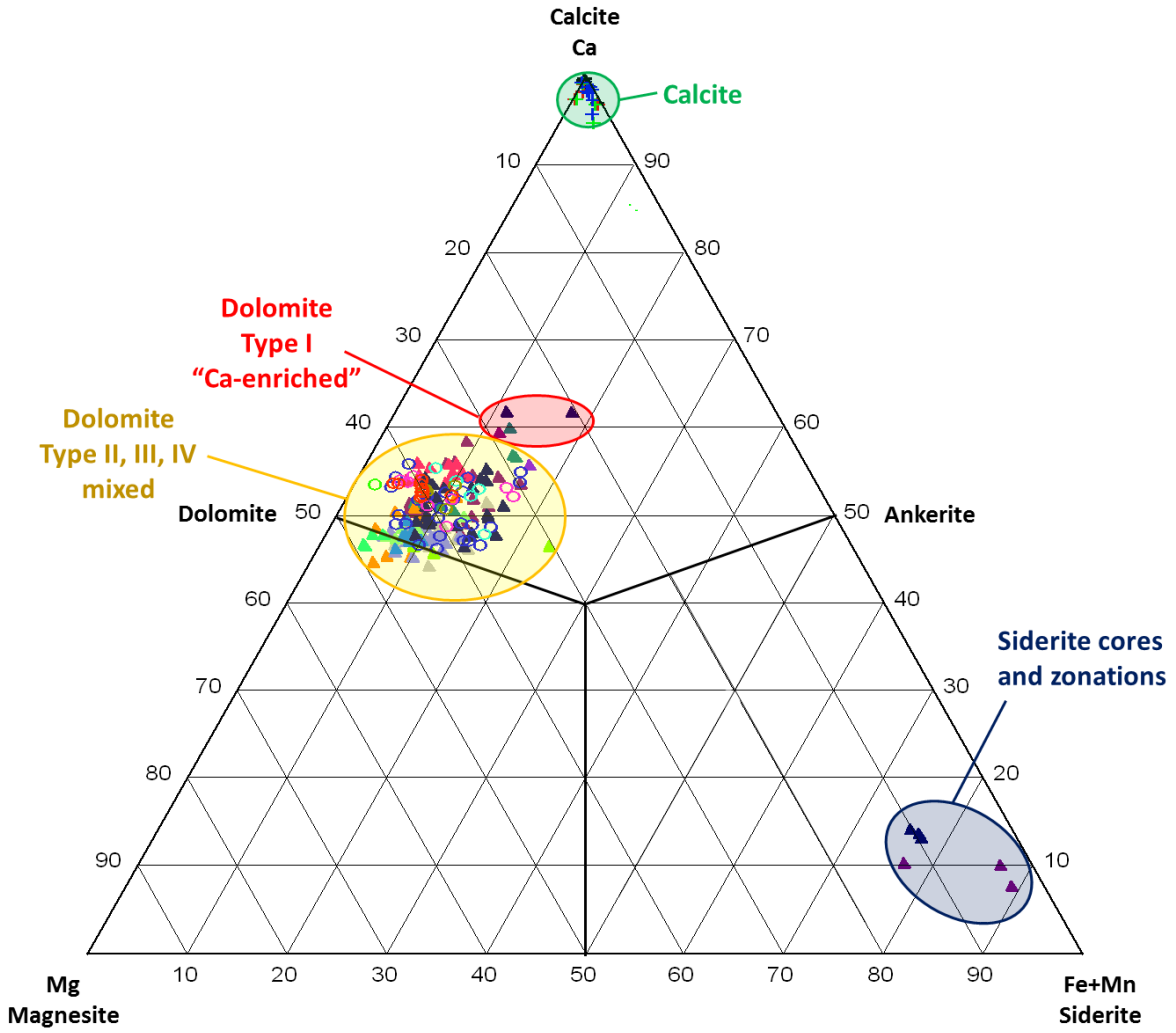

Figure 9: Ternary diagram for 22 carbonate cemented sandstone samples (values expressed in atomic percent; see Table 1). All analyses performed by means of EPMA. Triangles and circles are referring to samples recovered from the Zoovch Ovoo depocenter, whereas crosses are referring to samples recovered from outcrops located at Bayanshiree Plateau and East Hongor Tolgoy.

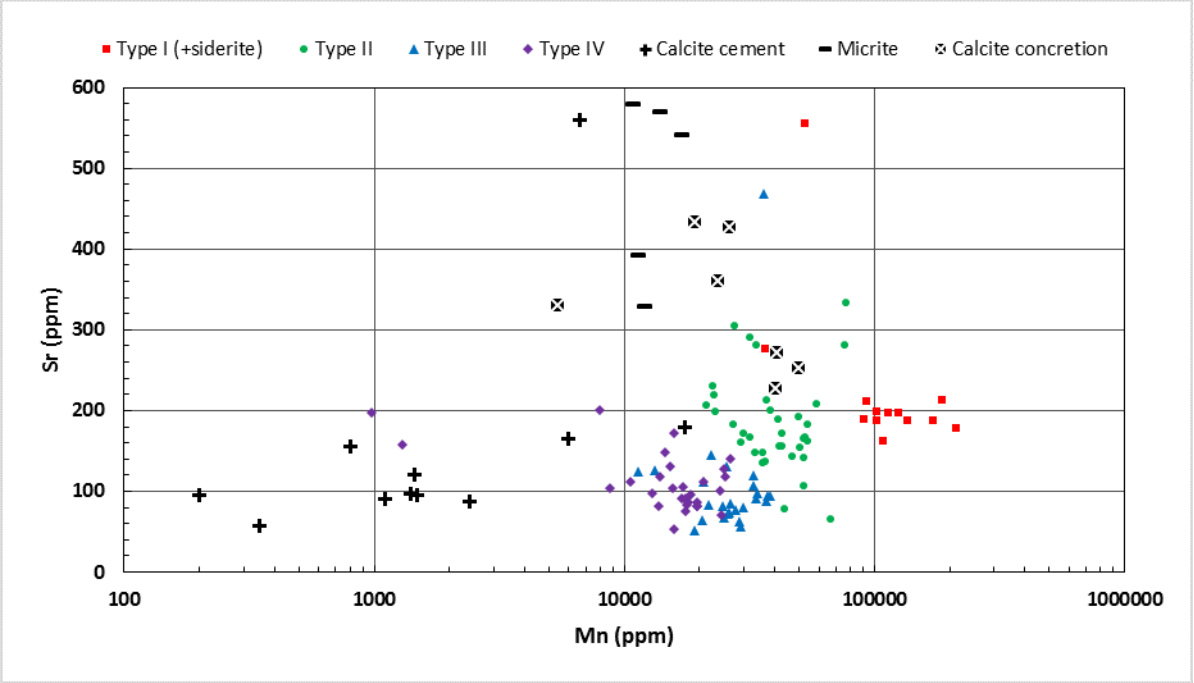

Figure 10: Sr versus Mn binary diagram with plot of the LA-ICP/MS data obtained for the dolomite and calcite (logarithmic values of Mn), in ppm (Table A1). A strong and gradual depletion in Mn and to some extent in Sr can be noticed within each dolomite group and successively from microcrystalline (Type I) plus siderite to the euhedral and poecilitic (Type II), subhedral (Type III) and anhedral (Type IV),. The three calcite groups, the calcite cement (calcite cemented sandstone), the micrite (microcrystalline <4µm) and the calcite concretion (pure calcite) show strong depletion patterns for Mn and Sr.

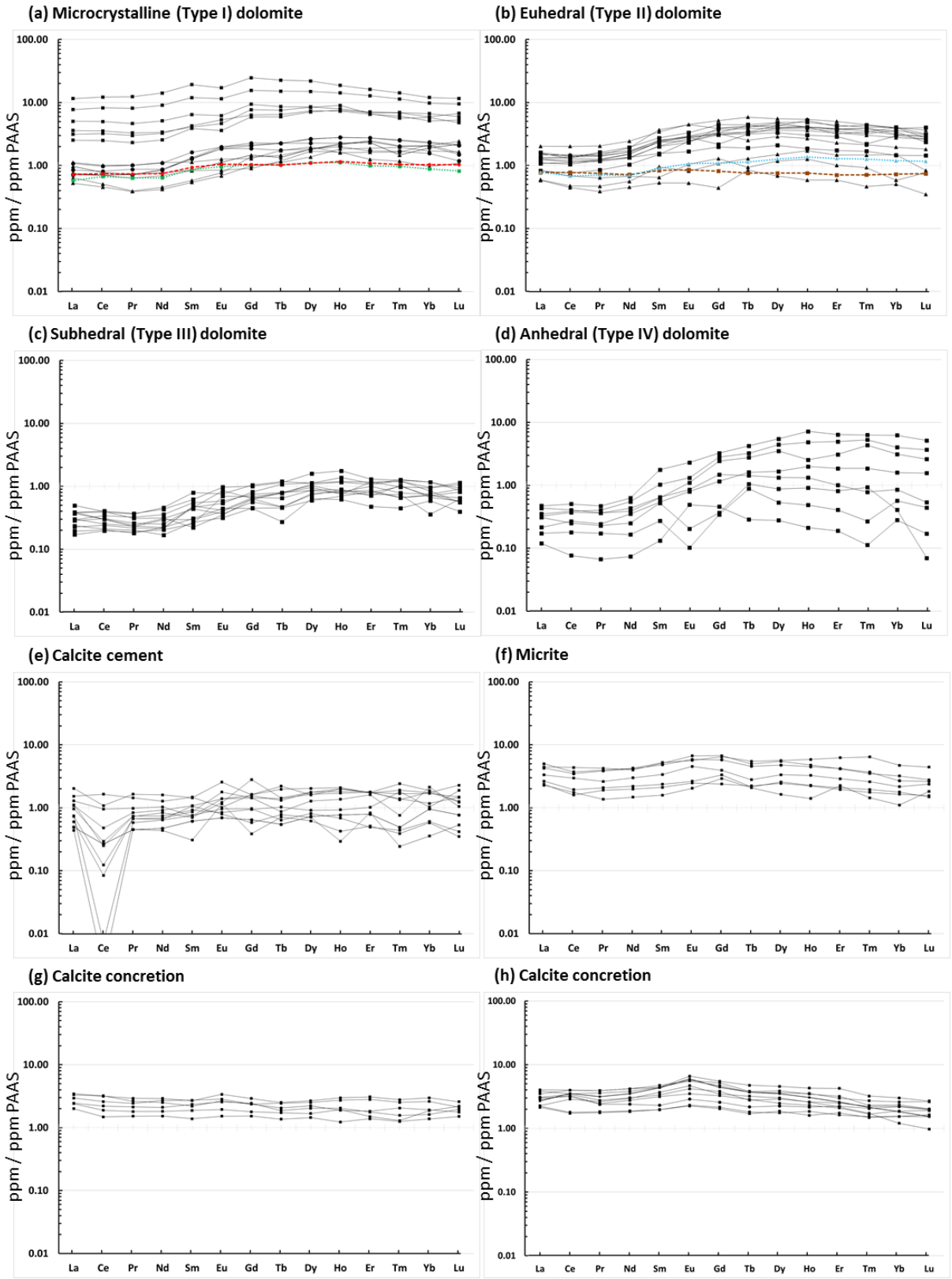

Figure 11: The REE spectra of the four dolomite fabrics and the calcite outcrops (PAAS-normalized); (a) microcrystalline (Type I) dolomite, in particular (i) patches in between poecilitic crystals (squares), (ii) patches with siderite (circles), (iii) uniform cement with sand grains not

in contact (triangles). The REE spectra of the bulk rock for (i) is represented as red rounded dots and for (ii) as green dash dots; (b) euhedral (Type II) dolomite, in particular: (i) poecilitic crystals (squares) and (ii) single rhombohedral crystals (triangles). The REE spectra of the bulk rock for (i) is represented as teal dash dots and for (ii) as brown rounded dots; (c) subhedral (Type III) dolomite; (d) anhedral (Type IV) dolomite; (e) calcite cement (sparite crystals); (f) micrite with sand grains not in contact; (g, h) calcite concretion (pure calcite without any sand grains). The numerical data of the above spectra are available in Table A2.

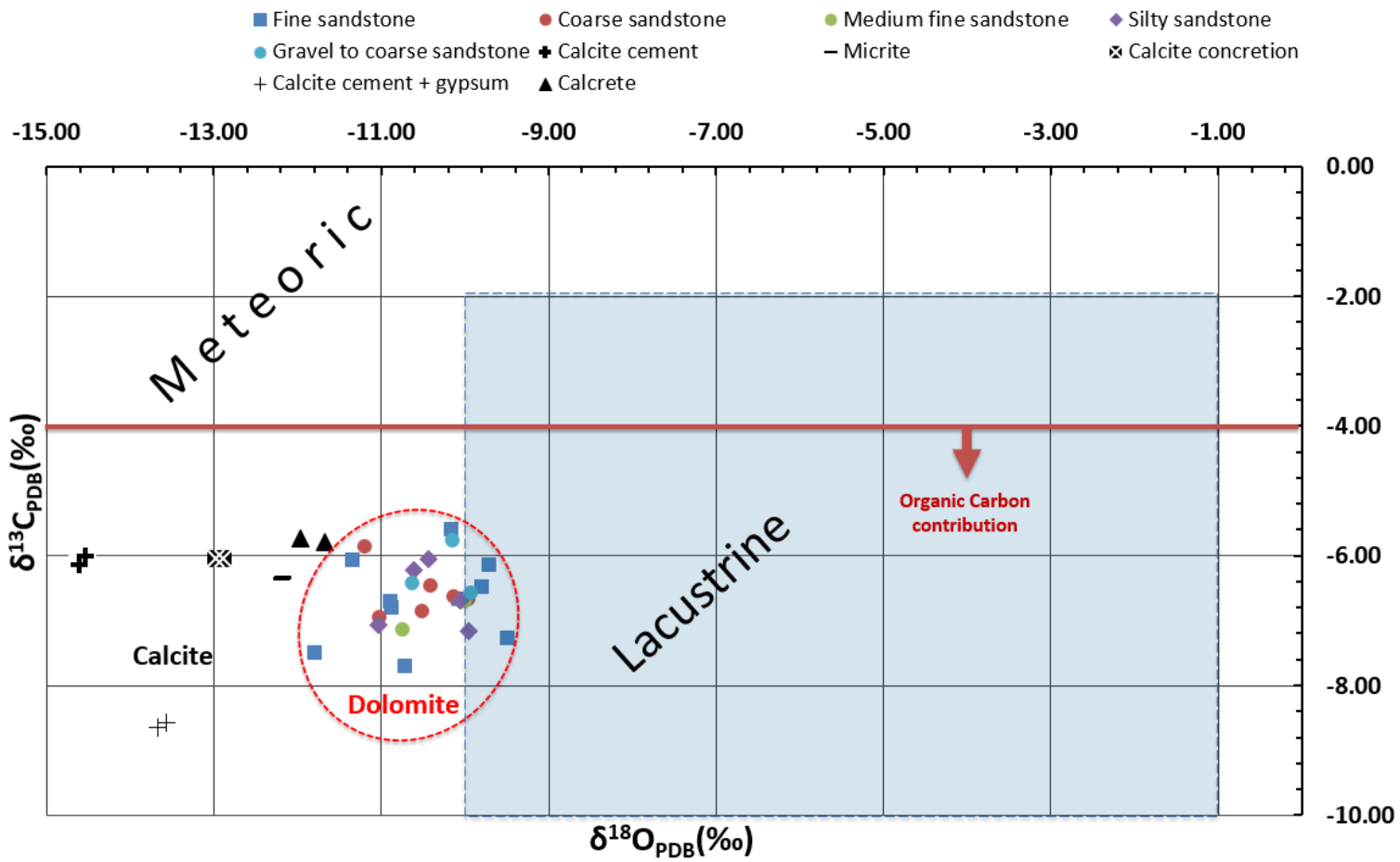

Figure 12: The isotopic composition of the dolomite and calcite cements. The reference fields for meteoric and lacustrine water are based on Hofer et al. (2013); organic-inorganic carbon fields according to Köster and Gilg (2015). Calcite cements present slightly higher $\delta^{18}O$ values than dolomite cements. The numerical data plotted above are available in Table 2. (For interpretation of the references to colour in this figure legend, the reader is referred to the web version of this article).

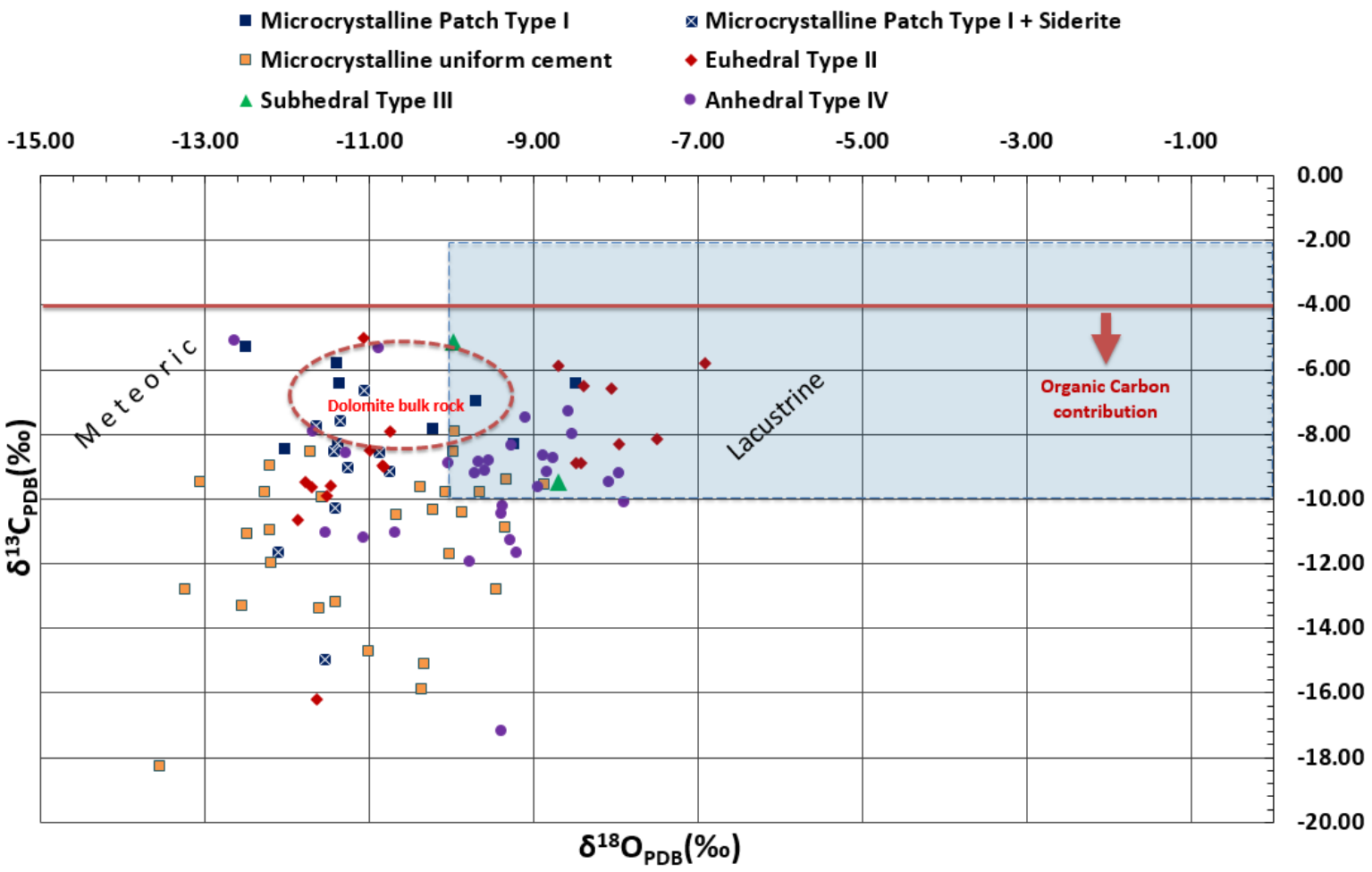

Figure 13: The isotopic composition of the dolomite and calcite cements for *in situ* measurements using SIMS. The bulk rock dolomite stable isotopes of Figure 12 area is discriminated by the red dashed line. The mean average of $\delta^{13}C$ and $\delta^{18}O$ for each dolomite type is provided in Table 3.

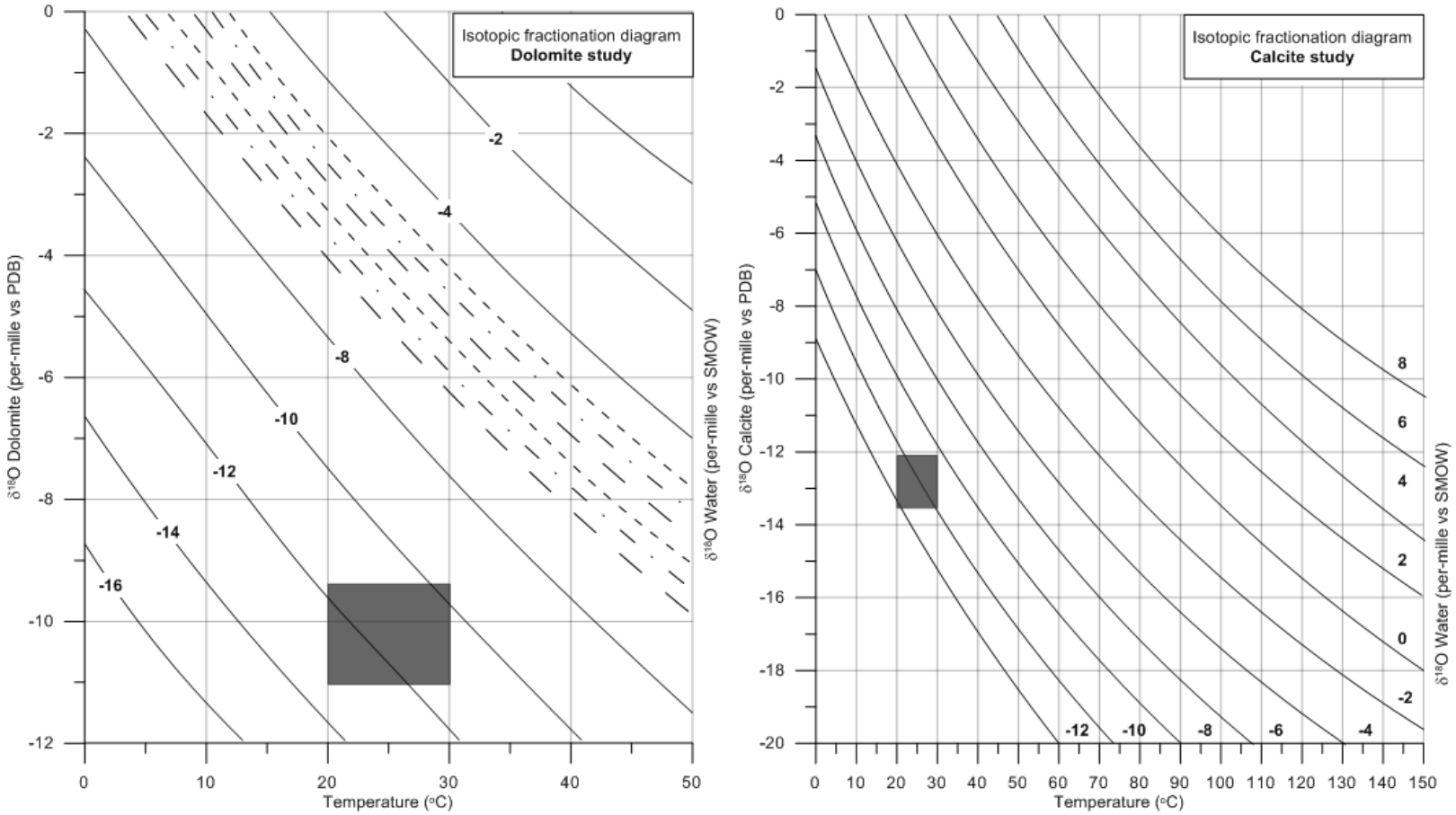

Figure 14: Diagrams of oxygen isotope equilibrium fractionation for the dolomite-water (Köster and Gilg, 2015) and calcite-water (Barbier et al. 2016). The curves represent the water $\delta^{18}O_{V\text{-}SMOW}$ values. For dolomite (left), the dotted, dotted-dashed and dashed lines represent oxygen isotope data of palustrine, ground and pedogenic waters as discussed in Köster and Gilg, 2015. Oxygen isotopic values for water in equilibrium with either dolomite or calcite were calculated for an estimated maximum temperature range of 20-30°C according to the burial history from Prost (2004).

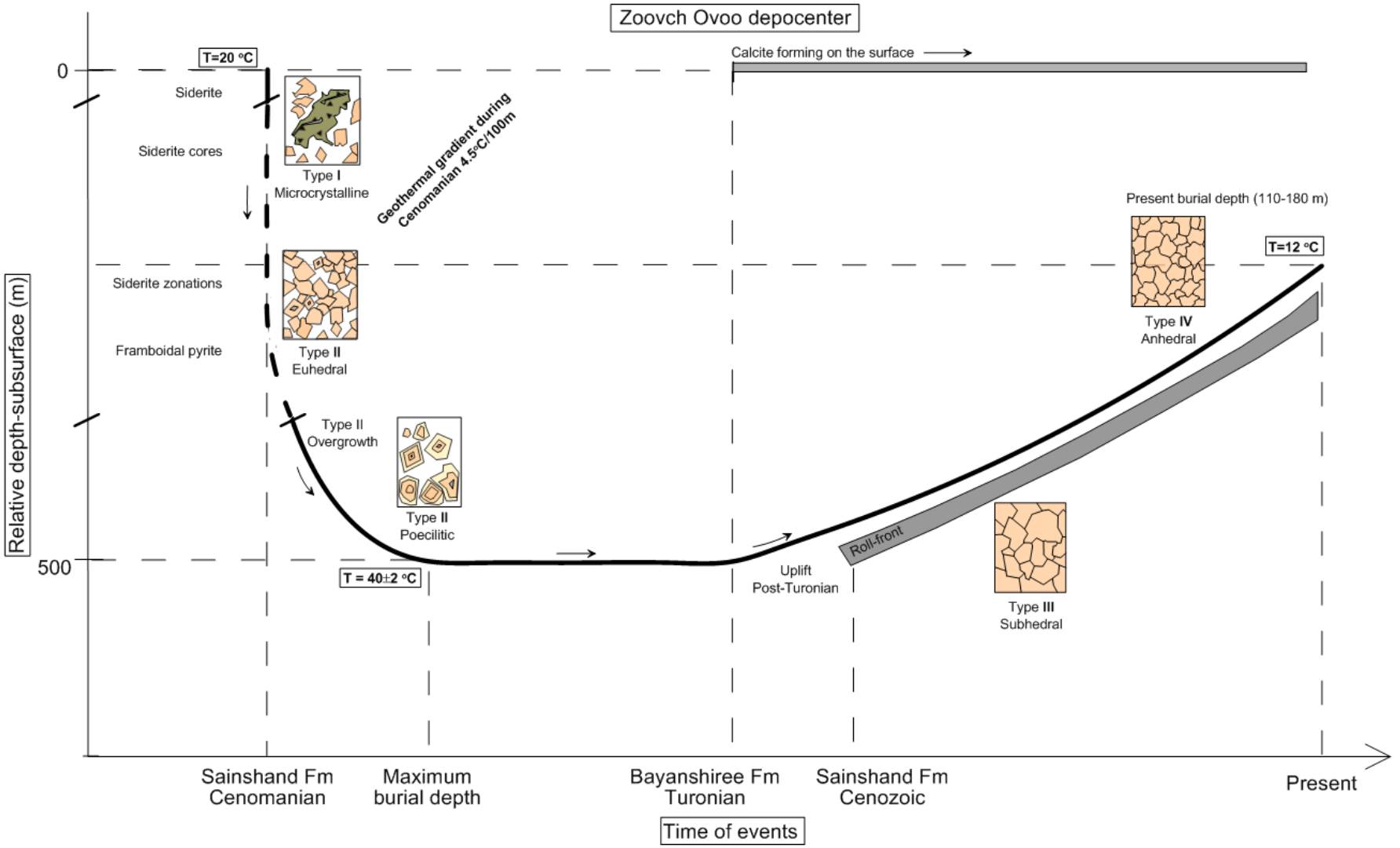

Figure 15: Proposed model for the dolomite cement evolution in Sainshand Formation of Zoovch Ovoo. Surface temperature and geothermal gradient according to Prost (2004). The black arrows indicate evolution with burial through stratigraphic time.

Tables

Table 1: Electron microprobe analysis (EPMA) of selected (representative) dolomite cements from Sainshand Formation and calcite cements from Bayanshiree Formation, expressed in atomic percent, projected on the ternary diagram of Figure 9. All values over the detection limit (0.02 at%).

at%	**9606-49**	**9606-53**	**9606-71**	**9606-72**	**9606-118**	**A-147**	**A-157**	**A-171**	**B-67**	**B-71**
Ca	25.67	24.21	26.31	26.47	26.74	27.19	28.34	25.94	25.70	23.76
Mg	18.51	19.69	17.57	18.07	21.16	15.71	14.33	19.96	17.01	20.29
Fe	3.77	4.57	2.42	2.71	1.07	3.09	3.58	2.60	2.74	2.80
Mn	1.61	1.26	2.52	2.37	0.89	3.88	3.49	1.30	4.37	3.11
Total	49.56	49.73	48.82	49.62	49.86	49.87	49.74	49.80	49.82	49.96
at%	**B-88**	**B-121**	**B-138**	**B-143**	**A-177**	**C-6**	**K-1**	**K-2**	**K-3A**	**K-3B**
Ca	24.19	22.88	23.36	24.09	26.90	6.51	49.71	48.86	48.62	48.42
Mg	19.91	21.21	24.41	21.55	20.37	4.72	0.14	0.54	1.07	0.27
Fe	2.39	5.33	0.83	2.10	1.12	26.64	0.02	0.03	0.02	0.00
Mn	2.24	0.57	1.31	2.10	1.33	11.19	0.11	0.32	0.18	1.05
Total	48.73	49.99	49.91	49.84	49.72	49.06	49.98	49.75	49.89	49.74

Table 2: Bulk stable carbon and oxygen isotopes for the dolomite (in depth) and calcite (surface) cements. Samples K-1 for calcite cement, K-2 for micrite, K-3A, K-3B for calcite concretion, K-4 for calcite cement associated to gypsum and K-6, K-7 for calcrete. For each sample the analysis was repeated twice for consistency. The data presented here are the mean values.

Sample	Borehole	Stage/lithology	Formation	Depth (m)	$\delta^{18}O$ (PDB)	$\delta^{18}O$ (SMOW)	$\delta^{13}C$ (PDB)	% Carbonate
A-36	710-7	Cenomanian	Sainshand	120.05	-11.34	19.17	-6.08	24.8
A-147	682-2	Cenomanian	Sainshand	141.50	-10.16	20.39	-5.59	31.4
A-157	676-2	Cenomanian	Sainshand	149.61	-10.43	20.11	-6.06	32.2
A-171	670-2	Cenomanian	Sainshand	168.29	-9.79	20.77	-6.48	36.3
A-177	989-5	Cenomanian	Sainshand	173.75	-10.88	19.64	-6.71	41.4
B-25	147-9	Cenomanian	Sainshand	153.92	-10.14	20.41	-5.78	16.9
B-37	364-11	Cenomanian	Sainshand	149.05	-10.06	20.49	-6.70	21.9
B-66	259-4a	Cenomanian	Sainshand	155.60	-10.87	19.65	-6.80	40.4
B-67	259-4b	Cenomanian	Sainshand	156.25	-11.79	18.71	-7.51	43.0
B-71	259-8	Cenomanian	Sainshand	165.65	-9.93	20.62	-6.58	57.1
B-78	351-5	Cenomanian	Sainshand	154.71	-9.96	20.59	-7.16	39.5
B-88	180-10	Cenomanian	Sainshand	182.10	-11.02	19.50	-6.95	28.7
B-91	180-13	Cenomanian	Sainshand	186.56	-10.40	20.14	-6.44	26.2
B-97	360-4	Cenomanian	Sainshand	174.72	-11.04	19.48	-7.08	43.2
B-110	213-6	Cenomanian	Sainshand	175.34	-11.25	19.26	-7.13	42.0
B-121	593-7	Cenomanian	Sainshand	175.26	-11.32	19.19	-5.86	18.7
B-125	593-11	Cenomanian	Sainshand	181.00	-9.48	21.09	-7.27	37.4
B-126	593-12	Cenomanian	Sainshand	182.54	-9.71	20.85	-6.15	38.9
B-129	886-2	Cenomanian	Sainshand	192.46	-10.62	19.91	-6.42	31.1
B-133	886-6	Cenomanian	Sainshand	200.80	-10.51	20.03	-6.87	29.6

B-135	886-8	Cenomanian	Sainshand	210.45	-10.62	19.91	-6.23	2.8
B-137	886-10	Cenomanian	Sainshand	212.68	-10.00	20.55	-6.71	30.7
B-138	886-11a	Cenomanian	Sainshand	215.85	-10.10	20.45	-6.65	22.1
B-139	886-11b	Cenomanian	Sainshand	216.20	-10.14	20.41	-6.63	21.6
B-148	895-9	Cenomanian	Sainshand	217.70	-9.96	20.59	-6.68	22.8
C-57	1100-9	Cenomanian	Sainshand	177.35	-10.71	19.82	-7.71	39.7
K-1	Outcrop	Turonian	Bayanshiree	-	-14.56	15.85	-6.09	34.4
K-2	Outcrop	Turonian	Bayanshiree	-	-12.18	18.30	-6.34	61.2
K-3	Outcrop	Turonian	Bayanshiree	-	-12.94	17.52	-6.04	80.9
K-4	Outcrop	Turonian	Bayanshiree	-	-13.62	16.82	-8.61	39.5
K-6	Outcrop	Turonian	Bayanshiree	-	-11.97	18.52	-5.74	57.6
K-7	Outcrop	Turonian	Bayanshiree	-	-11.68	18.82	-5.79	69.7

A, B, C = dolomite; K = calcite

Table 3: *In situ* analysis for carbon and oxygen stable isotopes for the dolomite cements in depth. The data presented here are the mean values for every dolomite type.

Sample	Borehole	Depth (m)	No of meas.	$\delta^{18}O$ (SMOW)	Stdev	$\delta^{18}O$ (PDB) mean	Stdev	$\delta^{13}C$ (PDB) mean	Stdev	Dolomite Type
B-71A	259-8	165.65	8	19.54	1.03	-11.04	1.00	-8.31	2.22	Microcrystalline patch type I
A-147	682-2	141.50	11	19.22	0.38	-11.35	0.37	-9.31	2.31	Microcrystalline grain + siderite
B-71B	259-8	165.65	31	19.16	2.05	-11.41	1.99	-11.56	2.70	Microcrystalline uniform cement
A-171	670-2	168.29	10	20.67	1.78	-9.94	1.72	-8.62	2.40	Euhedral
9704-10	738-1	139.45	9							
B-126	593-12	182.54	2	21.29	0.93	-9.35	0.91	-7.30	3.07	Subhedral
B-138	886-11a	215.85	7	20.99	1.21	-9.64	1.17	-9.46	2.22	Anhedral
B-71B	259-8	165.65	22							

Table 4: Paragenesis of dolomite cements encountered in the sands of the Sainshand formation of Zoovch Ovoo.

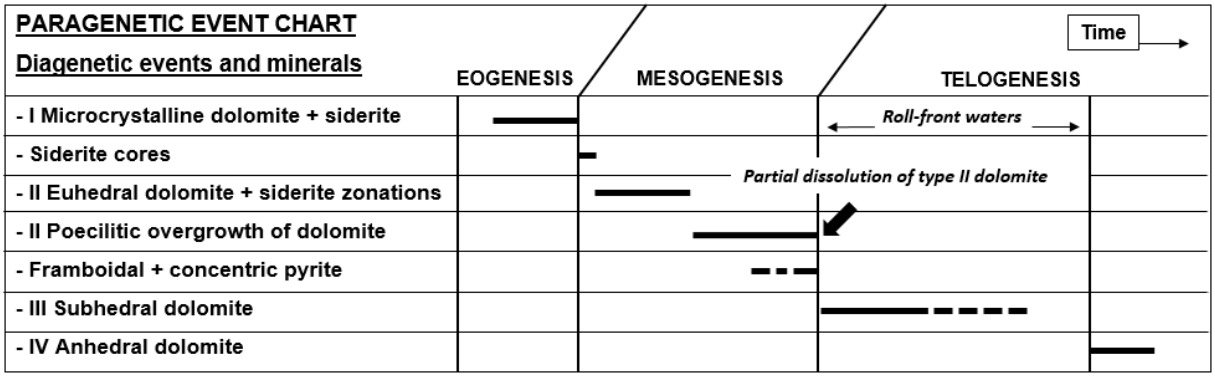

APPENDIX "Supplemental files"

Table A1: The Mn and Sr content of the four dolomite and three calcite types recognized in the studied dataset, projected on Figure 10, analyzed by LA/ICP-MS, expressed in ppm. All values over detection limit (10 ppm).

LA/spot	1	2	3	4	5	6	7	8	9	10	11
Microcrystalline (Type I) Dolomite + Siderite											
Mn	125000	101500	171000	113000	102400	92200	135600	90700	211000	185200	108100
Sr	197.4	188.6	188.6	197.8	199	211	187.5	189.4	179	213	161.9
Euhedral (Type II) Dolomite											
Mn	52810	53600	53600	33600	23070	49700	31700	41500	35700	29820	46900
Sr	166.7	183.9	162.4	162.4	198.6	193	291	156	149	172.2	143.7
Mn	22900	58400	27310	31700	76000	76800	52100	27600	52300	29200	35700
Sr	220	208.6	183.9	167	282	333	165.8	306	107.7	161.8	135.2
Mn	50400	43630	36700	33300	52200	66500	41250	21280	38340	36800	42500
Sr	155	78.2	136.8	148.8	142	65.2	189.7	207.3	200.6	213.7	155.7
Subhedral (Type III) Dolomite											
Mn	36230	22300	19100	32830	24900	20660	20540	26600	34000	36800	33540
Sr	469	145.6	50.9	119.6	68.2	112.2	64.9	85.4	98	88.4	91.8
Mn	11400	29900	32960	37540	38200	29200	25900	25660	26200	13210	28840
Sr	123.9	80.8	107.3	94.1	94.5	57	71.5	130.8	74	125.9	62.6
Anhedral (Type IV) Dolomite											
Mn	19490	17550	15790	19570	17860	17190	17970	17650	19440	16860	18340
Sr	81.6	90.5	53.5	81.4	83.6	105.8	86.2	74.8	86	92	95.3
Mn	26420	25200	15630	20600	25020	15290	10630	8790	14560	24190	24370
Sr	140	119	103.6	111.8	127.6	131.6	111.7	103.6	147.9	100.8	71.2
Mn	1294	8000	12940	13700	970	13900	15720	-	-	-	-
Sr	157.9	200	97.1	82	198	119	172.1	-	-	-	-
Calcite cement											
Mn	6600	2400	200	1100	1490	346	802	17500	1450	1390	5990
Sr	560	88	96	90	96	58	155	179	121	97	164
Micrite											
Mn	13800	17000	14800	11200	12010	11380	10800	10410	-	-	-
Sr	570	542	800	675	329	393	579	682	-	-	-
Calcite concretion											
Mn	5400	23630	8060	5480	6460	19100	6730	7720	49600	9190	9450
Sr	331	361	782	688	652	433	718	741	253	741	767
Mn	11040	16700	7600	40720	40130	26100	7810	-	-	-	-
Sr	751	698	937	272	227	427	943	-	-	-	-

Table A2: REE content (PAAS-normalized) of the four dolomite and three calcite fabrics (expressed in ppm), for in situ analysis. (*) indicates bulk rock analysis. Samples A-147, A-171, B-71 first group for microcrystalline dolomite; A-177, A-157 second group for euhedral dolomite; B-71, B-91 third group for subhedral dolomite; B-88 fourth group for anhedral dolomite. Samples K-1 for calcite cement, K-2 for micrite and K-3A, K-3B for calcite concretion.

Sample	La	Ce	Pr	Nd	Sm	Eu	Gd	Tb	Dy	Ho	Er	Tm	Yb	Lu
Microcrystalline (Type I) Dolomite														
A-147*	0.72	0.75	0.74	0.74	0.94	1.05	1.03	1.02	1.09	1.15	1.09	1.04	1.03	1.03
A-147	0.73	0.70	0.72	0.87	1.32	1.96	2.12	2.24	2.66	2.79	2.75	2.50	2.28	2.08
A-147	0.71	0.70	0.72	0.84	1.29	1.86	2.05	2.25	2.62	2.81	2.75	2.55	2.36	2.14
A-147	1.08	0.97	1.01	1.09	1.62	1.97	2.27	2.26	2.26	2.26	2.40	2.01	2.02	1.49
A-147	0.85	0.81	0.87	0.87	1.27	1.85	1.86	1.75	1.83	1.99	1.71	1.68	1.56	1.19
A-171*	0.58	0.67	0.63	0.64	0.86	0.96	1.02	1.03	1.11	1.12	0.99	0.97	0.88	0.82
A-171	3.59	3.54	3.28	3.39	4.05	4.63	7.68	7.53	8.38	8.99	6.63	5.63	5.78	4.77
A-171	7.72	8.23	8.12	9.06	11.93	11.48	15.58	15.13	14.96	14.16	12.77	11.37	9.75	9.51
A-171	11.57	12.16	12.34	14.13	19.24	17.13	24.76	22.60	21.92	18.69	16.18	14.22	11.99	11.58
A-171	2.52	2.49	2.31	2.55	3.89	3.59	5.90	5.94	7.12	7.58	6.95	6.83	5.89	6.72
A-171	5.03	5.00	4.64	5.10	6.43	6.19	9.38	8.60	8.50	7.90	7.05	6.93	6.67	5.95
A-171	3.12	3.22	3.00	3.25	4.27	5.31	6.31	6.43	7.33	7.30	6.49	6.10	5.11	5.26
B-71	0.75	0.70	0.63	0.69	0.83	0.84	0.90	1.18	1.69	1.63	1.25	1.17	0.96	1.09
B-71	1.12	1.01	1.01	1.12	1.14	1.26	1.29	1.73	1.97	1.60	1.62	1.63	2.13	1.58
B-71	0.97	0.77	0.72	0.77	0.85	1.12	1.46	1.34	1.82	2.21	2.32	1.46	1.91	2.16
B-71	0.52	0.45	0.39	0.42	0.54	0.69	0.99	1.12	1.37	1.84	1.87	1.95	1.70	1.65
B-71	0.63	0.51	0.39	0.45	0.58	0.77	1.37	1.45	1.79	2.13	2.49	2.05	2.06	2.42
Euhedral (Type II) Dolomite														
A-177*	0.77	0.78	0.75	0.72	0.84	0.85	0.81	0.76	0.76	0.76	0.71	0.71	0.73	0.74
A-177	1.52	1.40	1.39	1.64	2.52	2.87	3.30	4.31	3.97	4.10	3.82	3.88	3.16	2.81
A-177	0.84	0.68	0.64	0.68	0.65	1.05	1.29	0.94	1.18	1.26	1.01	0.93	0.59	0.77
A-177	1.26	1.14	1.16	1.32	2.04	2.66	3.28	3.36	3.65	3.59	3.26	3.02	2.77	2.63
A-177	2.02	2.01	2.04	2.43	3.42	4.47	5.15	5.86	5.53	5.41	5.02	4.46	4.01	3.65
A-177	1.57	1.30	1.26	1.53	2.34	2.44	3.22	2.51	2.88	2.69	2.29	2.12	1.95	1.81
A-177	1.49	1.48	1.46	1.92	3.68	4.44	3.86	4.03	4.70	4.05	3.19	3.41	3.97	2.74
A-177	0.58	0.44	0.39	0.45	0.53	0.53	0.44	0.84	0.68	0.59	0.59	0.46	0.50	0.35
A-177	0.59	0.48	0.47	0.56	0.95	0.81	1.07	1.29	1.50	1.71	1.47	1.46	1.49	0.84
A-177	1.52	1.40	1.39	1.64	2.52	2.87	3.30	4.31	3.97	4.10	3.82	3.88	3.16	2.81
A-157*	0.78	0.68	0.71	0.70	0.91	1.07	1.09	1.14	1.27	1.37	1.30	1.26	1.19	1.17
A-157	1.30	1.32	1.56	1.71	2.47	2.94	3.61	3.86	3.89	3.89	3.47	3.20	3.62	3.09
A-157	1.34	1.36	1.62	1.94	2.74	3.32	4.46	4.45	4.79	4.87	4.35	4.05	4.04	3.14
A-157	1.08	1.12	1.22	1.51	2.41	2.83	3.09	3.40	4.29	4.09	3.72	3.88	3.44	2.35
A-157	1.26	1.20	1.21	1.34	1.55	1.67	1.97	1.90	2.09	1.86	1.73	1.68	1.46	1.44
A-157	1.60	1.43	1.44	1.63	2.32	2.80	2.17	3.16	3.31	3.03	2.88	2.20	2.98	2.65
A-157	0.82	0.76	0.85	1.04	1.50	2.41	3.07	3.21	3.95	4.05	3.79	3.56	3.05	2.98
A-157	1.10	1.05	1.20	1.35	2.00	2.31	3.91	4.29	4.25	5.20	4.14	4.37	3.90	4.00
Subhedral (Type III) Dolomite														
B-71	0.23	0.21	0.20	0.17	0.27	0.31	0.45	0.45	0.59	0.70	0.82	0.66	0.72	0.65
B-71	0.30	0.25	0.23	0.22	0.31	0.44	0.45	0.27	0.63	0.62	0.48	0.45	0.59	0.40
B-71	0.49	0.40	0.31	0.31	0.22	0.35	0.62	0.78	0.96	0.75	1.17	1.20	0.96	1.14
B-71	0.37	0.30	0.23	0.29	0.30	0.40	0.64	0.47	0.76	0.82	0.86	0.66	0.73	0.57
B-71	0.39	0.30	0.24	0.31	0.44	0.36	0.56	0.47	0.73	0.86	0.80	1.00	0.71	0.81
B-91	0.38	0.39	0.36	0.46	0.79	0.76	1.05	1.19	1.12	1.37	1.11	1.27	1.16	0.86
B-91	0.39	0.40	0.37	0.43	0.62	0.97	1.01	1.14	1.59	1.76	1.30	1.24	1.16	0.93
B-91	0.19	0.20	0.18	0.22	0.46	0.85	0.64	0.79	1.03	0.82	0.99	0.78	0.75	0.91
B-91	0.28	0.31	0.26	0.25	0.46	0.54	0.81	1.08	1.13	1.19	1.17	0.98	0.94	1.07
B-91	0.23	0.24	0.22	0.21	0.49	0.42	0.66	0.65	0.87	0.89	0.71	1.02	0.67	0.58
B-91	0.29	0.34	0.32	0.36	0.55	0.58	0.75	0.79	0.86	0.78	0.74	0.73	0.36	0.63
B-91	0.09	0.10	0.11	0.13	0.18	0.18	0.34	0.32	0.60	0.75	0.59	0.56	0.18	0.63

B-91	0.17	0.20	0.19	0.20	0.26	0.69	0.68	0.78	1.07	1.16	1.07	1.22	0.83	0.56
Anhedral (Type IV) Dolomite														
B-88	0.31	0.25	0.23	0.25	0.52	0.20	0.36	1.05	0.88	0.91	0.81	0.93	0.41	0.07
B-88	0.17	0.18	0.17	0.17	0.27	0.10	0.34	0.88	0.53	0.48	0.41	0.27	0.57	0.44
B-88	0.43	0.40	0.36	0.43	0.65	0.85	1.48	1.43	1.33	1.32	1.00	0.78	0.85	0.53
B-88	0.12	0.08	0.07	0.07	0.13	0.49	0.46	0.29	0.28	0.21	0.19	0.11	0.28	0.17
B-88	0.35	0.39	0.40	0.55	1.03	1.31	2.81	3.23	4.42	4.83	4.95	5.27	4.01	3.67
B-88	0.21	0.27	0.24	0.35	0.54	0.80	1.16	1.61	1.67	1.99	1.86	1.85	1.60	1.56
B-88	0.32	0.37	0.37	0.39	0.63	1.10	2.42	2.77	3.50	2.54	3.09	4.34	3.12	2.60
B-88	0.47	0.51	0.47	0.63	1.77	2.31	3.24	4.23	5.45	7.17	6.39	6.29	6.24	5.14
Calcite														
K-1	1.02	0.69	0.71	1.00	0.56	1.94	0.60	0.17	1.52	0.91	0.67	2.20	0.96	1.00
K-1	1.29	0.95	0.98	1.03	0.74	1.39	1.57	1.31	1.75	2.02	1.76	2.41	1.88	1.26
K-1	0.60	0.08	0.67	0.66	1.06	0.80	0.58	0.78	0.71	0.29	0.83	0.24	0.35	0.53
K-1	1.12	0.25	0.72	0.83	0.70	1.21	2.81	1.43	1.77	1.81	1.79	1.34	1.77	1.23
K-1	0.73	0.12	0.67	0.68	0.86	1.78	1.44	0.87	1.28	1.36	1.61	0.76	2.13	1.05
K-1	0.96	0.29	0.74	0.74	0.92	0.84	0.94	1.03	0.91	0.93	1.02	1.80	1.03	1.88
K-1	2.03	1.08	1.64	1.61	1.44	2.56	1.61	1.97	2.03	2.09	1.72	1.90	1.74	2.28
K-1	1.53	1.65	1.44	1.27	1.48	1.01	1.63	2.21	1.60	1.98	1.75	1.39	1.17	1.47
K-1	0.49	0.27	0.45	0.47	0.61	0.69	0.64	0.55	0.73	0.77	0.79	0.49	0.96	0.77
K-1	0.44	0.00	0.45	0.44	0.31	1.16	0.39	0.71	0.62	0.42	0.51	0.39	0.58	0.35
K-1	0.74	0.01	0.58	0.64	0.76	0.96	0.97	0.64	0.81	0.69	0.49	0.44	0.60	0.42
K-1	1.08	0.48	0.84	0.91	1.08	1.39	1.44	1.40	1.64	1.71	1.76	1.68	1.70	1.48
K-2	2.28	1.75	1.36	1.47	1.59	2.04	2.92	2.08	1.62	1.40	2.25	1.44	1.10	1.81
K-2	3.32	2.95	2.62	2.98	3.37	4.54	3.93	2.79	3.33	3.26	2.88	2.59	2.16	2.37
K-2	5.00	3.71	3.96	4.25	5.23	5.65	6.44	5.45	5.62	5.86	6.25	6.41	4.72	4.42
K-2	4.45	4.35	4.22	3.98	5.10	6.67	6.72	4.95	5.45	4.75	4.14	3.49	3.19	2.77
K-2	1.16	0.62	0.71	0.75	0.76	0.85	1.07	0.69	0.81	0.98	0.87	1.05	0.82	0.83
K-2	2.36	1.60	1.90	1.97	2.11	2.48	2.38	2.22	2.44	2.22	1.95	1.76	1.64	1.56
K-2	2.63	1.93	2.07	2.19	2.36	2.63	3.33	2.13	2.56	2.26	2.07	1.95	1.77	1.49
K-2	4.26	3.47	3.85	4.17	4.83	5.83	5.77	4.55	4.76	4.48	4.18	3.66	2.68	2.63
K-3A	3.45	3.20	2.63	2.50	2.20	2.65	2.36	2.44	2.52	2.72	2.80	2.51	2.60	2.12
K-3A	3.32	3.16	2.92	2.90	2.68	3.38	2.90	2.51	2.67	2.98	3.08	2.78	2.98	2.58
K-3A	2.94	2.59	2.43	2.70	2.72	2.83	2.36	2.05	2.22	1.89	1.82	2.05	1.91	1.77
K-3A	2.45	2.20	2.13	2.09	2.34	2.56	2.43	1.87	2.03	2.04	1.77	1.56	1.62	1.95
K-3A	2.41	1.88	1.80	1.81	1.87	1.94	1.78	1.73	1.68	1.94	1.49	1.29	1.86	2.19
K-3A	2.45	1.89	1.77	1.29	2.00	0.84	1.52	1.96	0.94	1.27	2.84	1.32	2.23	2.05
K-3A	2.22	1.76	2.05	1.56	2.04	2.04	2.38	2.22	1.35	1.55	1.09	1.88	0.74	2.14
K-3A	1.99	1.48	1.52	1.53	1.38	1.52	1.53	1.36	1.45	1.23	1.39	1.25	1.38	1.50
K-3B	2.70	3.56	3.13	3.50	4.34	5.99	4.42	3.71	3.49	3.05	2.60	2.13	1.83	1.54
K-3B	2.14	1.73	1.76	1.83	1.96	2.25	2.04	1.70	1.86	1.60	1.74	1.48	1.54	1.63
K-3B	2.23	1.79	1.82	1.88	1.97	2.31	2.15	1.81	1.76	1.85	1.62	1.53	1.54	1.53
K-3B	3.09	3.41	2.75	3.02	3.35	4.18	3.82	2.77	2.89	2.61	2.50	2.20	2.24	2.00
K-3B	2.85	3.28	2.42	2.76	3.15	3.49	3.26	2.86	2.48	2.30	2.09	1.68	1.87	1.91
K-3B	4.03	3.99	3.93	4.19	4.72	5.65	5.21	3.82	3.87	3.45	3.19	2.29	2.34	2.02
K-3B	2.27	2.88	2.63	2.95	3.69	4.68	3.45	3.21	3.01	2.58	2.16	1.72	1.20	0.98
K-3B	3.50	3.96	3.90	4.19	4.40	6.59	5.49	4.74	4.57	4.29	4.24	3.22	3.01	2.69
K-3B	3.03	3.16	2.38	2.40	2.31	2.88	2.58	2.17	2.24	2.16	2.22	2.06	2.20	1.95
K-3B	3.83	3.50	3.59	3.81	4.43	5.57	4.70	3.70	3.63	3.54	2.98	2.71	2.60	2.63